IOP Publishing Plasma Sources Science and Technology
Plasma Sources Sci. Technol. **30** (2021) 065025 (20pp) https://doi.org/10.1088/1361-6595/abfbc7

The role of negative hydroxyl ions in the electron generation and breakdown during plasma formation in liquid water

Ali Charchi Aghdam and Tanvir Farouk*

Department of Mechanical Engineering, University of South Carolina, Columbia, SC 29208, United States of America

E-mail: tfarouk@sc.edu

Received 16 February 2021, revised 13 April 2021
Accepted for publication 26 April 2021
Published 24 June 2021

Abstract

The role of negative hydroxyl ions in liquid-phase plasma discharge formation is investigated using an inhouse modeling framework. Two tunneling sources for electrons are considered—tunneling ionization of water molecules and tunneling detachment of negative hydroxyl ions together with additional reaction steps. The simulations are conducted for a needle-like powered electrode with two different nanosecond rise time voltage profiles—a linear and an exponential rise. Both the profiles have a maximum voltage of 15 kV. The predictions show that the electron detachment, which has a much lower threshold energy requirement, provides a stream of electrons at low applied voltage during the initial rise time. The electrical forces from the electron detachment process generate stronger compression but a weaker expansion regime in the liquid resulting in ∼40% increase in the density and only ∼1% decrease. The electron detachment tunneling process is found to be not limited by the electric field, but rather by the availability of negative hydroxyl ions in the system and ceases when these ions are depleted. The tunnel ionization of water molecules forms the electron wave at a higher applied voltage, but the resulting peak electron number density is typically six orders of magnitude larger than the detachment tunneling. The higher electron number density allows the recycling of depleted negative hydroxyl ions in the system and can reestablish tunneling detachment. In addition, the system experiences a larger variation in density; specifically, a decrease in density due to tunnel ionization. The prediction also shows that irrespective of the initial electron sources (i.e. tunnel ionization or tunnel detachment) the reduced electric field is not sufficient enough to allow electron impact ionization to be active and make a significant contribution. Path flux analysis is conducted to determine the kinetics responsible for the recycling of the negative hydroxyl ions.

Keywords: plasma in liquid, breakdown, tunneling, negative hydroxyl ions

(Some figures may appear in colour only in the online journal)

1. Introduction

Plasma discharges in liquids is a relatively new field [1]. These discharges have attracted a lot of attention in recent years due to their distinctive properties—highly non-equilibrium nature, ultrahigh density, high reactivity and unique chemical selectivity. These discharges offer a plethora of new physical and chemical effects resulting in exotic reactions in the liquid phase and gas–liquid interfaces at room temperature, which drive the inception of several novel technologies. In recent years, the applications of non-thermal interfacial plasmas have increased exponentially, driven by breakthroughs in biological and biomedical technologies [2], material/particle synthesis [3], plasma supported electrolysis [4, 5], fuel reform-

* Author to whom any correspondence should be addressed.

ing [6] and waste water treatment [7]. Canonical well-defined experiments have been conducted to understand the initiation process of liquid-phase plasma discharges [2]. To suppress ohmic heating and associated phase change in most experiments, high voltage with fast rise times is used. In addition, limiting the pulse rise and duration/length time to a few nanoseconds supposedly minimizes the fluid interaction near the vicinity of the electrode. The inertia of the fluid is too high to respond to the fast voltage rise and the short pulse duration. Experimental characterization of these nanosecond liquid-phase plasma discharges has been conducted by various groups [8–12]. Despite the large number of experimental studies, modeling and simulations on this topic is limited.

The mechanism responsible for plasma initiation in liquid medium varies depending on the type of the discharge [9, 13–15] and, as a result, remains a topic of contention. The two mechanisms that are generally highlighted for the electrical breakdown in liquids are electron multiplication in the liquid phase and breakdown associated with low-density regions in the liquid acting as nucleation sites. Many processes have been identified that could result in the formation of the low-density region in the liquids—Joule heating contributing to localized evaporation [16], electrostrictive effects causing the liquid to rupture and form nanovoids under high and fast rising electric fields when the absolute value of the negative pressure is greater than 30 MPa (cavitation threshold) [17], and pre-existing bubbles near the powered electrode due to possible degassing [18]. For electron multiplication in the liquid phase, the density of the medium is so high that the creation of a typical electron avalanche by satisfying the Townsend criterion is very unlikely due to the strong scattering of the electrons. Field-dependent ionization through Zener tunneling has been proposed as the possible source of ionization and breakdown in transformer oils [19], a concept which has been extended to describe breakdown in liquid water as well [20, 21]. The recent experimental study conducted by von Keudell and his group [15] is supportive of the field-ionization-driven breakdown.

Field-ionization-driven breakdown of liquid water is underpinned by the concept that the lack of strong lattice structure in liquids allows ionization of water molecules through the Zener tunneling process which is possible at lower threshold values [22]. However, Shneider and Pekker [23] suggest that the probability of electron detachment from negative OH^-_{aq} ions, is higher than the probability of field ionization of water molecules and this detachment can also take place at a lower energy barrier. The field dependent ionization of a water molecule is generally expressed by the following formula [20, 21]:

$$Z_{H_2O_{aq}}(\mathbf{E}) = n_{H_2O_{aq}} \frac{q|\mathbf{E}|d}{h} \exp\left(-\frac{m_e d\pi^2\Delta^2}{q|\mathbf{E}|h^2}\right), \qquad (1)$$

where $n_{H_2O_{aq}}$ is the number density of water, q is the electron charge, $\mathbf{E}$ is the electric field, d is the molecular separation distance, h is Planck's constant, m_e is the effective electron mass and Δ (4 eV) is the ionization energy barrier for water. It should be noted that due to limited theoretical studies on liquid-phase ionization processes, the Zener mechanism of ionization of liquid water and the adopted parameters for calculating the probability of tunneling are a hypothesis.

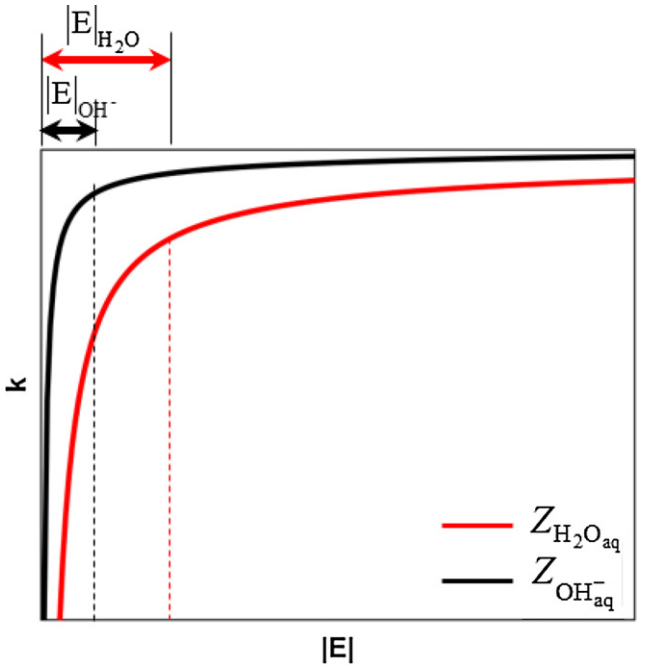

Figure 1. A schematic presentation and comparison of rate constants of field-dependent ionization of H_2O_{aq} and tunneling detachment of electrons from OH^-_{aq} as a function of electric field magnitude.

The tunneling detachment of electrons from OH^-_{aq} ions can be expressed in the following form [23]:

$$Z_{OH^-_{aq}}(\mathbf{E}) = n_{OH^-_{aq}} \frac{\pi A^2 q|\mathbf{E}|}{\sqrt{2I_n m_e}} \exp\left(-\frac{4}{3}\frac{\sqrt{2m_e}}{qh}\frac{I_n^{3/2}}{|\mathbf{E}|}\right), \qquad (2)$$

where $n_{OH^-_{aq}}$ is the number density of OH^-_{aq} ions in the liquid, and I_n is the affinity energy of an electron in a negative ion (1.85 eV). The coefficient $A \sim 1$ depends on the shape of the potential well.

Figure 1 compares the rate of electron formation from H_2O_{aq} and OH^-_{aq} through the tunneling process. Even though the ionization energy barrier is significantly lower (4 eV) in the tunneling process, an even lower threshold energy for the tunneling detachment allows electron formation from OH^-_{aq} to be effective at a lower electric field. An obvious question arises: are there sufficient OH^-_{aq} available in the liquid phase to participate in the electron? OH^-_{aq} ions are present in water due to the self-ionization equilibrium reaction, $H_2O_{aq} \rightleftharpoons H^+_{aq} + OH^-_{aq}$. Under ambient conditions (i.e. atmospheric pressure and 298 K), the self-ionization reaction can result in an equilibrium ion density of $n_{H^+_{aq}} = n_{OH^-_{aq}} = 6 \times 10^{19}$ m^{-3} in distilled water. Shneider [23] infers that the number of electrons formed by field detachment from OH^-_{aq} ions in a cubic micron of water in 1 ns is $\sim n_e > 15$ and proposes that seed electrons for the liquid-phase breakdown can be generated through this route. However, in their estimation they have only considered the existing equilibrium OH^-_{aq} ions and subsequent

Table 1. Different species considered in the model[a].

Electrons	e, e_{aq}
Ions	H^+, H^-, OH^-, O^-, H_2O^+, OH^-_{aq}, O^-_{aq}, $O^-_{2,aq}$, $O^-_{3,aq}$, $H_2O^+_{aq}$, $HO^-_{2,aq}$, $H_3O^+_{aq}$
Neutrals	H, H_2, OH, H_{aq}, $H_{2,aq}$, OH_{aq}, O_{aq}, $O_{2,aq}$, $O_{3,aq}$, H_2O_{aq}, $HO_{2,aq}$, $H_2O_{2,aq}$

[a] *aq*: aqueous.

generation of OH^-_{aq} driven by an external electric field; associated electron and charged species kinetics are neglected. In the presence of a strong field, the number of electrons generated through this channel may increase significantly. Furthermore, the fast rate of electron detachment from OH^-_{aq} suggests that under electrical pulses that have a few nanoseconds rise and decay time, the OH^-_{aq} concentration can decrease and recycling pathways could contribute to the replenishment of the OH^-_{aq} ions.

In this work, a previously developed mathematical modeling framework together with an extended kinetic model is employed to simulate the plasma discharge formation in liquid water. The primary objective of this study is to investigate the role of both ionization and detachment of electrons due to Zener tunneling and its overall impact on the initial stage of the plasma discharge development. To be consistent with our prior work, we studied two different voltage-driving conditions: a linear and an exponential ramp(s).

2. Mathematical model

The mathematical model consists of the fluid dynamic equations of the mass, momentum and energy conservations for the bulk medium in compressible form, species conservation equations for each of the species considered (electrons, positive ions, negative ions, radicals and neutrals) and the Poisson's equation for the electric field. A local field approximation is employed to determine the electron temperature as a function of the reduced electric field ($|\mathbf{E}|/N$). A brief description of the model is provided here, and details are reported in [21].

The mass, momentum and energy conservation of a compressible Newtonian fluid is described by the following equations:

$$\frac{\partial \rho}{\partial t} + \nabla \cdot (\rho \mathbf{U}) = 0, \tag{3}$$

$$\frac{\partial \rho \mathbf{U}}{\partial t} + \nabla \cdot (\rho \mathbf{U} \cdot \mathbf{U}) = \mu \nabla^2 \mathbf{U} - \nabla p + \mathbf{F}, \tag{4}$$

$$\frac{\partial \rho E_{\text{tot}}}{\partial t} + \nabla \cdot (\rho \mathbf{U} E_{\text{tot}}) + \nabla \cdot (\mathbf{U} p) = -\nabla \cdot \mathbf{q} + \nabla \cdot (\tau \cdot \mathbf{U}) + \mathbf{J}_{\text{ion}} \cdot \mathbf{E}, \tag{5}$$

where ρ is the liquid density, $\mathbf{U}$ is the velocity vector, μ is the viscosity, p is the hydrodynamic pressure and $\mathbf{F}$ is the electrical force vector. In the energy conservation equation E_{tot} is the total energy, $\mathbf{q}$ is the conductive heat flux, τ is the viscous stress tensor and $\mathbf{J}_{\text{ion}}$ is the ion current density. The electric force vector $\mathbf{F}$ includes the contribution of electrostatic, polarization and electrostrictive ponderomotive forces. The Tait equation of state [24] is used to relate the pressure to the density of water.

The general species transport equation employed has the following form:

$$\frac{\partial n_k}{\partial t} + \nabla \cdot (n_k \mathrm{U}) + \nabla \cdot (\pm \mu_k \mathbf{E} n_k) = \nabla \cdot (D_k \nabla n_k) + \dot{n}_k, \tag{6}$$

where n_k is the number density of the k^{th} species, μ_k and D_k are the mobility and the diffusion coefficient for k^{th} species, respectively, and $\dot{n}_k$ is the source term. The species transport equation also considers the flux of species due to the bulk fluid motion. It should be noted that for neutrals and radicals the drift flux is not considered.

Assuming the liquid medium is a dense gas, the electron mobility and diffusivity are obtained as a function of the reduced electric field $|\mathbf{E}|/N$ from the solution of a zero-dimensional Boltzmann equation [25]. The diffusion coefficient of solvated electrons (e_{aq}) is prescribed to be 4.74×10^{-9} m^2 s^{-1} [26] and the mobility is obtained from the Einstein relationship.

Diffusion coefficients of the ions are determined using the Nernst–Einstein equation [27]:

$$D_k = \frac{RT}{z_k^2 F^2}, \tag{7}$$

where R is the gas constant, T is the temperature, Z_k is the charge number, F is Faraday's constant and $\Lambda^0_{m,k}$ is the limiting molar conductivity of the ion. The diffusion coefficients are used to determine the ion mobility using the Einstein relationship.

The diffusivity of the neutrals and radicals are estimated by employing the Stokes–Einstein equation [28]:

$$D_k = \frac{k_{\text{B}} T}{6\pi \mu r_0}, \tag{8}$$

where k_{B} is Boltzmann's constant, μ is the solvent viscosity and r_0 is the solute radius.

Standard no-slip and zero-gradient boundary conditions are utilized for velocity and density, respectively, at all the boundaries. For the energy equation, an adiabatic wall boundary condition is prescribed. The electric potential at the grounded electrode is set to zero and a time varying potential representative of a nanosecond pulse is prescribed at the powered electrode. Flux boundary conditions are used for species at the electrodes and a secondary electron emission coefficient of 0.01 is set [21].

Table 2. The water reaction mechanism[a].

#	Reaction	Rate	Reference
R1	$H_2O_{aq} \rightarrow H_2O^+ + e$	$Z_{H_2O}\left(\lvert\mathbf{E}\rvert\right)$	[20]
R2	$OH^-_{aq} \rightarrow OH + e$	$Z_{OH}\left(\lvert\mathbf{E}\rvert\right)$	[23]
R3	$e + H_2O_{aq} \rightarrow OH^- + H$	$f(\lvert\mathbf{E}\rvert/N)$	[30]
R4	$e + H_2O_{aq} \rightarrow H_2 + O^-$	$f(\lvert\mathbf{E}\rvert/N)$	[30]
R5	$e + H_2O_{aq} \rightarrow OH + H^-$	$f(\lvert\mathbf{E}\rvert/N)$	[30]
R6	$e + H_2O_{aq} \rightarrow H_2O^+ + 2e$	$f(\lvert\mathbf{E}\rvert/N)$	[30]
R7	$H_2O^+ + e \rightarrow H_2O_{aq}$	1.0×10^{-19}	[20]
R8	$e + H_2O_{aq} \rightarrow e_{aq} + H_2O_{aq}$	3.3×10^{-18}	[29]
R9	$H + H_2O_{aq} \rightarrow H_{aq} + H_2O_{aq}$	5.0×10^{-21}	[29]
R10	$H_2 + H_2O_{aq} \rightarrow H_{2,aq} + H_2O_{aq}$	5.0×10^{-21}	[29]
R11	$O^- + H_2O_{aq} \rightarrow O^-_{aq} + H_2O_{aq}$	5.0×10^{-21}	[29]
R12	$OH + H_2O_{aq} \rightarrow OH_{aq} + H_2O_{aq}$	5.0×10^{-21}	[29]
R13	$H^+ + H_2O_{aq} \rightarrow H_3O^+_{aq}$	5.0×10^{-21}	[29]
R14	$OH^- + H_2O_{aq} \rightarrow OH^-_{aq} + H_2O_{aq}$	5.0×10^{-21}	[29]
R15	$H_2O^+ + H_2O_{aq} \rightarrow H_2O^+_{aq} + H_2O_{aq}$	5.0×10^{-21}	[29]
R16	$e_{aq} + H_2O_{aq} \rightarrow H_{aq} + OH^-_{aq}$	3.2×10^{-26}	[29]
R17	$e_{aq} + H_2O^+_{aq} \rightarrow H_{aq} + OH_{aq}$	1.0×10^{-15}	[29]
R18	$2e_{aq} + 2H_2O_{aq} \rightarrow H_{2,aq} + 2OH^-_{aq}$	9.1×10^{-18}	[29]
R19	$e_{aq} + H_{aq} + H_2O_{aq} \rightarrow H_{2aq} + OH^-_{aq}$	6.9×10^{-44}	[29]
R20	$e_{aq} + OH_{aq} \rightarrow OH^-_{aq}$	5.0×10^{-17}	[29]
R21	$e_{aq} + O^-_{aq} + H_2O_{aq} \rightarrow 2OH^-_{aq}$	6.1×10^{-44}	[29]
R22	$e_{aq} + H_3O^+_{aq} \rightarrow H_{aq} + H_2O_{aq}$	3.8×10^{-17}	[29]
R23	$e_{aq} + H_2O_{2,aq} \rightarrow OH_{aq} + OH^-_{aq}$	1.8×10^{-17}	[29]
R24	$e_{aq} + HO^-_{2,aq} + H_2O_{aq} \rightarrow OH_{aq} + 2OH^-_{aq}$	9.7×10^{-45}	[29]
R25	$e_{aq} + O_{2,aq} \rightarrow O^-_{2,aq}$	3.2×10^{-17}	[29]
R26	$e_{aq} + O_{aq} \rightarrow O^-_{aq}$	3.2×10^{-17}	[29]
R27	$H_{aq} + H_2O_{aq} \rightarrow H_{2,aq} + OH_{aq}$	1.7×10^{-26}	[29]
R28	$H_{aq} + H_{aq} \rightarrow H_{2,aq}$	1.2×10^{-17}	[29]
R29	$H_{aq} + OH_{aq} \rightarrow H_2O_{aq}$	1.2×10^{-17}	[29]
R30	$H_{aq} + OH^-_{aq} \rightarrow e_{aq} + H_2O_{aq}$	3.7×10^{-20}	[29]
R31	$H_{aq} + H_2O_{2,aq} \rightarrow OH_{aq} + H_2O_{aq}$	1.5×10^{-19}	[29]
R32	$H_{2,aq} + H_2O_{2,aq} \rightarrow H_{aq} + OH_{aq} + H_2O_{aq}$	1.0×10^{-20}	[29]
R33	$H_{aq} + O_{2,aq} \rightarrow HO_{2,aq}$	3.5×10^{-17}	[29]
R34	$H_{aq} + HO_{2,aq} \rightarrow H_2O_{2,aq}$	1.7×10^{-17}	[29]
R35	$O_{aq} + H_2O_{aq} \rightarrow 2OH_{aq}$	2.2×10^{-23}	[29]
R36	$O_{aq} + O_{2,aq} \rightarrow O_{3,aq}$	5.0×10^{-18}	[29]
R37	$OH_{aq} + OH_{aq} \rightarrow H_2O_{2,aq}$	9.1×10^{-18}	[29]
R38	$OH_{aq} + O^-_{aq} \rightarrow HO^-_{2,aq}$	3.3×10^{-17}	[29]
R39	$OH_{aq} + H_{2,aq} \rightarrow H_{aq} + H_2O_{aq}$	7.0×10^{-20}	[29]
R40	$OH_{aq} + OH^-_{aq} \rightarrow O^-_{aq} + H_2O_{aq}$	2.2×10^{-17}	[29]
R41	$OH_{aq} + HO_{2,aq} \rightarrow H_2O_{aq} + O_{2,aq}$	1.0×10^{-17}	[29]
R42	$OH_{aq} + O^-_{2,aq} \rightarrow OH^-_{aq} + O_{2,aq}$	1.3×10^{-17}	[29]
R43	$O^-_{aq} + H_2O_{aq} \rightarrow OH^-_{aq} + OH_{aq}$	3.0×10^{-21}	[29]
R44	$O^-_{aq} + H_{2,aq} \rightarrow OH^-_{aq} + H_{aq}$	1.3×10^{-19}	[29]
R45	$O^-_{aq} + H_2O_{2,aq} \rightarrow O^-_{2,aq} + H_2O_{aq}$	8.3×10^{-19}	[29]
R46	$O^-_{aq} + HO^-_{2,aq} \rightarrow O^-_{2,aq} + OH^-_{aq}$	6.6×10^{-19}	[29]
R47	$O^-_{aq} + O_{2,aq} \rightarrow O^-_{3,aq}$	6.0×10^{-18}	[29]
R48	$O^-_{aq} + O^-_{2,aq} + H_2O_{aq} \rightarrow 2OH^-_{aq} + O_{2,aq}$	1.7×10^{-45}	[29]
R49	$OH_{aq} + H_2O_{2,aq} \rightarrow H_2O_{aq} + HO_{2,aq}$	4.5×10^{-20}	[29]
R50	$OH_{aq} + HO^-_{2,aq} \rightarrow OH^-_{aq} + HO_{2,aq}$	1.2×10^{-17}	[29]
R51	$H_2O^+_{aq} + H_2O_{aq} \rightarrow H_3O^+_{aq} + OH_{aq}$	1.0×10^{-23}	[29]
R52	$H_3O^+_{aq} + OH^-_{aq} \rightarrow H_{aq} + OH_{aq} + H_2O_{aq}$	1.0×10^{-16}	[29]
R53	$HO_{2,aq} + H_2O_{aq} \rightarrow H_3O^+_{aq} + O^-_{2,aq}$	3.3×10^{-24}	[29]
R54	$H_3O^+_{aq} + O^-_{2,aq} \rightarrow HO_{2,aq} + H_2O_{aq}$	1.0×10^{-25}	[29]

[a]Reaction rate constants: $m^3\ s^{-1}$ (first-order reactions) and $m^6\ s^{-1}$ (second-order reactions).

3. Kinetic model

The kinetic model contains both electron-induced and heavy particle reactions. The model consists of 26 species and 54 reactions. Table 1 provides an overview of the different species taken into account, and the reactions considered are summarized in table 2. Reactions R1 and R2 correspond to ionization of H_2O_{aq} and OH^-_{aq} by the tunneling process, respectively, and the associated reaction rates are described in equations (1) and (2). R3–R5 are dissociative attachment reactions, R6 is electron impact ionization, R7 is the electron–ion recombination reaction and R8–R15 are reactions associated with solvation of electrons and ions. Reactions involving solvated electrons participating in the liquid phase are considered as they do contribute to the formation of heavy particle charged species—more specifically OH^-_{aq} that allows electron multiplication through the tunneling process. R16–R54 represent aqueous reactions.

The rates for R3–R6 are calculated from gas-phase cross-section data employing a dense gas approximation. These reaction rates are determined using the zero-dimensional Boltzmann equation solver BOLSIG+ over a range of reduced electric ($|\mathbf{E}|/N$) and tabulated in the form of lookup tables. Rates for the solvation and aqueous reactions are obtained from [29]. It should be noted that the chemical kinetic model is developed for deionized, distilled water with no dissolved gases (e.g. nitrogen, oxygen).

4. Numerical scheme

The numerical scheme for solving the governing equations is based on the finite volume approach. The sets of equations are assembled and solved within the OpenFOAM framework [31]. The discretized equations are solved in a sequential manner. Details on the numerical schemes used for the flow field and species are presented in our prior publication [21]. Here, we present some of the newer implementations.

The rate constants of reactions can be a function of $|\mathrm{E}|$, $|\mathrm{E}|/N$ or can be a constant value. Generally, the electrical field cannot be assumed constant at each time step. Therefore, components of the electric field vector are assumed to vary in each cell in a linear fashion over each time step, i.e. $\mathbf{E}_j(t) = c_j t + d_j$, $j = x, y, z$; where j is the components of the electric field vector. Values of c_j are calculated by using the values of $\mathbf{E}_j$ at two consecutive times. The differential equation is then obtained as:

$$\begin{aligned}\frac{\mathrm{d}|\mathbf{E}|}{\mathrm{d}t} &= \frac{\mathrm{d}|\mathbf{E}|}{\mathrm{d}E_x}\frac{\mathrm{d}E_x}{\mathrm{d}t} + \frac{\mathrm{d}|\mathbf{E}|}{\mathrm{d}E_y}\frac{\mathrm{d}E_y}{\mathrm{d}t} + \frac{\mathrm{d}|\mathbf{E}|}{\mathrm{d}E_z}\frac{\mathrm{d}E_z}{\mathrm{d}t} \\ &= \sum_j c_j \frac{E_j}{|\mathbf{E}|} = \sum_j \frac{c_j\left(c_j t + d_j\right)}{\sqrt{\sum_k (c_k t + d_k)^2}} \qquad j,k = x,y,z.\end{aligned} \tag{9}$$

The initial value problem to be solved can be represented in the following vector format:

$$\mathbf{y}' = \mathbf{f}(\mathbf{y}) = \begin{bmatrix} \mathrm{d}n_0/\mathrm{d}t \\ \mathrm{d}n_1/\mathrm{d}t \\ \vdots \\ \mathrm{d}n_{N_s-1}/\mathrm{d}t \\ \mathrm{d}\,|\mathbf{E}|\,/\mathrm{d}t \end{bmatrix} = \begin{bmatrix} \dot{n}_0 \\ \dot{n}_1 \\ \vdots \\ \dot{n}_{N_s-1} \\ \sum_j c_j \dfrac{E_j(t)}{|\mathbf{E}(t)|} \end{bmatrix}, \tag{10}$$

where the vector of unknowns is $\mathbf{y} = [n_0, n_1, \ldots, n_{N_s-1}, |\mathbf{E}|]^T$.

In our prior simulation work, we only considered three reactions, all of which had very similar time scales. In this work, we considered a kinetic scheme that has reactions that possess significantly different time scales and therefore contribute to the 'stiffness' of the problem. 'Stiffness' does not allow the forward integration to converge in a reasonable computational time. To overcome this difficulty, an operator splitting method is employed. In the splitting scheme, the governing equation is split into sub-equations, usually with each having a single operator capturing only a portion of the physics present, and each is integrated separately and sequentially in time to advance to the next time step [32]. This allows the reaction source terms to be resolved with specialized solvers for stiff problems while maintaining a simple integration scheme for the transport terms. A brief and general outline of the splitting scheme is provided here.

In a general form, a time-dependent reaction–transport system can be described by the following nonlinear ordinary differential equation [32]:

$$\frac{\mathrm{d}\mathbf{r}}{\mathrm{d}t} = \mathbf{S}(\mathbf{r}) + \mathbf{M}(\mathbf{r}, t), \tag{11}$$

where $\mathbf{r}$ is the vector of dependent variables (here, species number densities and electric field), $\mathbf{S}(\mathbf{r})$ is the vector of rates of change of $\mathbf{r}$ due to chemical reactions and $\mathbf{M}(\mathbf{r}, t)$ is the vector of rates of change of $\mathbf{r}$ due to transport processes. Equation (11) is discretized in increments of Δt, and the integration in time is then performed using the Strang splitting scheme [33]. The splitting scheme separates the reaction term from the transport process and the numerical integration is performed in three sub-steps.

In sub-step 1, the reaction terms are integrated over a time interval of $\Delta t/2$ by solving:

$$\frac{\mathrm{d}\mathbf{r}^{\mathrm{a}}}{\mathrm{d}t} = \mathbf{S}(\mathbf{r}^{\mathrm{a}}). \tag{12}$$

The initial condition $\mathbf{r}^{\mathrm{a}}(0)$ is taken to be the final state $\mathbf{r}$ from the previous time step, and the solution to equation (12) is denoted by $\mathbf{r}(\Delta t/2)$.

In sub-step 2, the transport terms are integrated over a time interval Δt by solving:

$$\frac{\mathrm{d}\mathbf{r}^{\mathrm{b}}}{\mathrm{d}t} = \mathbf{M}(\mathbf{r}^{\mathrm{b}}, t). \tag{13}$$

The initial condition $\mathbf{r}^{b}(0)$ corresponds to the final state of the system from the previous sub-step, $\mathbf{r}^{a}(\Delta t/2)$, and the solution to equation (13) is denoted by $\mathbf{r}^{b}(\Delta t)$.

In the final sub-step (sub-step 3), an integration identical to sub-step 1 is performed taking the $\mathbf{r}^{b}(\Delta t)$ as the initial condition. At the completion of this sub-step, the final state of the system is given by $\mathbf{r}^{c}(\Delta t/2)$. This is the solution at the end of the current time step and serves as the initial condition for the next time step. It can be shown that if each of the three sub-steps in the above splitting procedure is solved with at least second-order accuracy in time, the Strang splitting scheme maintains a second-order accuracy [32].

In the proposed solution method, the integration of the reaction terms (sub-steps 1 and 3) is performed with an implicit backward differentiation formula (BDF) widely used for the integration of stiff reactive systems. The SUNDIALS (suite of nonlinear and differential/algebraic equation solvers) solver package [34] which has a variable-order, variable-step, multistep ODE solver based on BDF is coupled to the OpenFOAM solver. To solve the reaction terms, the CVODE solver from SUNDIALS is employed. In each flow time step integration (i.e. the step taken to solve the flow field, electric potential, etc) equation (10) is solved twice according to the Strang splitting procedure. BDF integration with the SPGMR (scaled, preconditioned, generalized minimum residual) linear solver is used in all calculations. Internal numerical approximation of the Jacobin matrix by SUNDIALS is used. Iterations are performed until a desired residual is attained.

5. Results and discussion

Simulations are conducted for a curved electrode configuration with two different voltage profiles—a linear ramp and a rapid pulse. A maximum voltage of 15 kV is considered. The sharp needle-like electrode is represented as a prolate ellipsoid with a radius of the electrode tip of 5 μm, and a ratio of the major to small semiaxis as 5. The electrode configuration has a minimum inter-electrode separation distance of 60 μm. A schematic of the computational domain and the temporal voltage profiles are presented in figure 2. The computational domain and applied voltage profiles are identical to the one used in our previous work [21]. To differentiate the role of electron source terms in the initiation process, three cases are simulated:

(a) Case I: electrons formed through ionization of water molecules via the Zener tunneling mechanism (all reactions in table 2 except R2).
(b) Case II: electrons formed through detachment from negative hydroxyl ions via the tunneling mechanism (all reactions in table 2 except R1).
(c) Case III: electrons formed through a combination of ionization of water molecules and detachment from hydroxyl ions via the tunneling mechanism.

The cases are determined by isolating the two different electron sources forming through the tunneling process (i.e. reactions R1 and R2) reactions to determine their independent role in the plasma dynamics. Impacts of both sources are simultaneously considered in case III to assess the combined effect. For these three cases both the linear and exponential ramp referred to as a 'pulse' are simulated.

Figures 3 and 4 present the spatiotemporal evolution of the axial velocity and density along the center line. For case I, both the linear ramp and pulse result in a flow reversal, which takes place at ~3 ns. At $t > 3$ ns a traveling wave front emerges with peak velocity of ~180 m s^{-1} and ~220 m s^{-1} for the linear ramp and pulse, respectively, maintaining a subsonic flow field. The variation in the center line density profiles for case I (figures 4(a) and (d)) shows that the density undergoes sharp variations. The compression and expansion regions are initiated at 3.50 ns with a sub-micron low-density region near the electrode surface followed by a high-density region. The density decreases and increases by ~12% and 15%, respectively. For the pulse, the low-density region extends further downstream (figure 4(d)). These velocity and density profiles are qualitatively similar to our prior work in which a three-step kinetic mechanism was considered, which included field ionization through the Zener tunneling process [21]. For case II, having OH^{-}_{aq} as the only ionization source (figures 3(b) and (e)) generates a distinctively different velocity distribution. The positive velocity region (i.e. the region where fluid moves away from the powered electrode) does not appear when OH^{-}_{aq} are the only source of the initial electrons. The velocity magnitude is similar to the case I condition. Electron detachment through tunneling results in neutral OH in the system and, unlike the H_2O ionization route, no positive charge is produced. As a result, the electrostatic force ($\mathbf{F_{es}}$) is low when electrons are detached from OH^{-}_{aq} during the initial stage (figure 5(b)). The flow field for case II is predominantly dictated by both the polarization ($\mathbf{F_{pol}}$) and ponderomotive ($\mathbf{F_{pon}}$) forces, unlike for case I in which all of $\mathbf{F_{es}}$, $\mathbf{F_{pol}}$ and $\mathbf{F_{pon}}$ have significant contributions. With initial electrons formed only through tunneling detachment, a compression wave near the powered electrode is formed (figures 4(b) and (e)). The density increases by ~40% as a result of compression. Unlike case I, in which a traveling compression is observed, in case II the compression region remains anchored to the powered electrode. The associated expansion results only in less than ~1% and ~5% decrease in density for a linear ramp (figure 4(b)) and pulse (figure 4(e)), respectively. The electron tunneling detachment forms extremely small low-density regions spatially, where the decrease in the density is also very minimal. The velocity and density profiles in the presence of both tunneling ionization and detachment (i.e. case III) are mainly dictated by the tunnel ionization process. Both the center-line velocity and density distribution (figures 3 and 4(c) and (f)) are very much similar to that of the profiles in case I.

The evolution of the electron number density (n_e) and OH^{-}_{aq} under the linear ramp conditions are presented in figure 5. The spatiotemporal evolution shows that due to lower threshold energy, the free electrons from OH^{-}_{aq} detachment (case

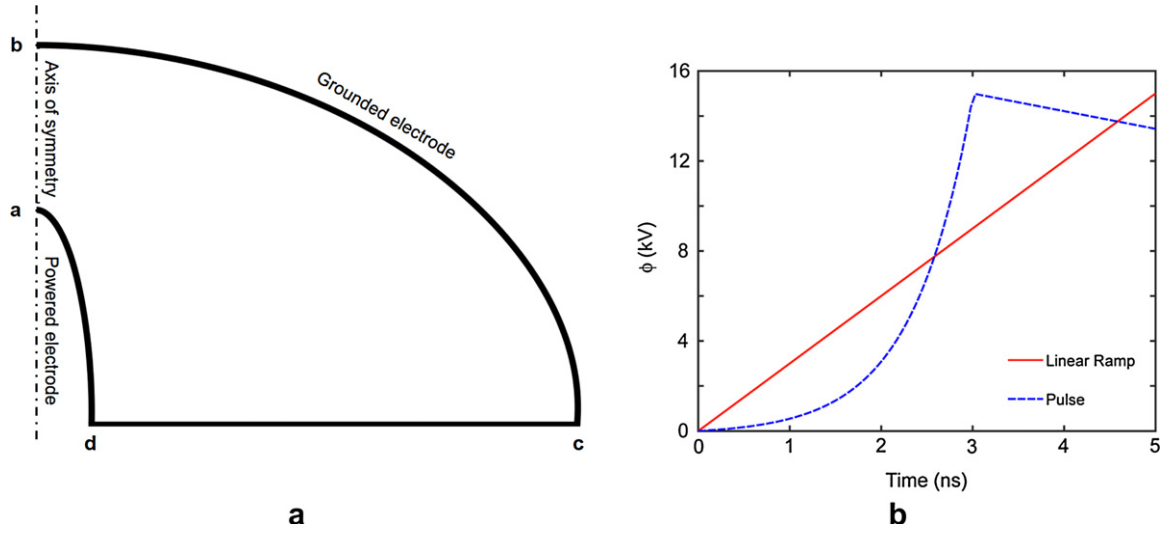

Figure 2. (a) A schematic of the problem geometry, and (b) the transient voltage profiles employed at the powered electrode.

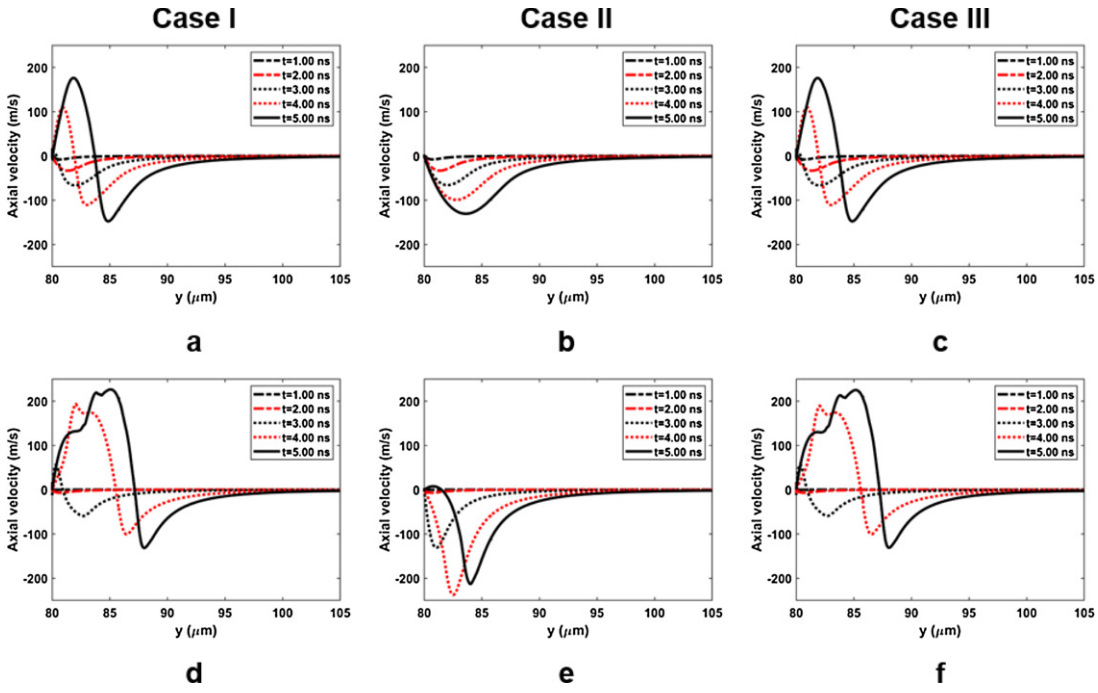

Figure 3. Temporal evolution of the centerline axial velocity for case I (a) and (d), case II (b) and (e) and case III (c) and (f). Viewgraphs in the top row (a)–(c) are for the linear voltage ramp and those in the bottom row (d)–(f) are under the pulsed profile.

II) are formed at earlier times compared to the H_2O tunnel ionization channel (case I). At $t = 1$ ns, as the driving voltage reaches 3 kV, the maximum n_e formed by reaction R2 is around 5×10^{18} m^{-3} and a propagating wave of n_e emerges near the vicinity of the powered electrode. In comparison, when the electrons are formed through H_2O ionization (i.e. reaction R1) under the same applied voltage, the maximum n_e is only $\sim 10^{12}$ m^{-3}. But at 2 ns, the peak n_e with only R1 active reaches a value of $\sim 10^{21}$ m^{-3}, whereas with only the R2 channel the peak n_e remains constant as the driving voltage continues to increase during the ramp up. In addition to the available electric field/electron energy, the R2 reaction rate is limited by the presence of available OH^-_{aq}. At the very initial stage, electrons are detached from the pre-existing hydroxyl ion OH^-_{aq} available in the water, which is 6×10^{19} m^{-3}. These negative hydroxyl ions are rapidly consumed through the R2 channel forming free electrons. This is evident in the OH^-_{aq} profile at $\sim$1 ns, which shows a sharp decrease in the OH^-_{aq} near the powered electrode. As the n_e wave front propagates forward, the OH^-_{aq} number density in the trailing downstream region continues to increase from the resulting aqueous and solvated electron reactions. The OH^-_{aq} formation routes generate sufficient negative ions to maintain a quasi-steady concentration. With electrons forming only through the R1 channel, the ionization wave does not appear to propagate until $\sim$4 ns (figure

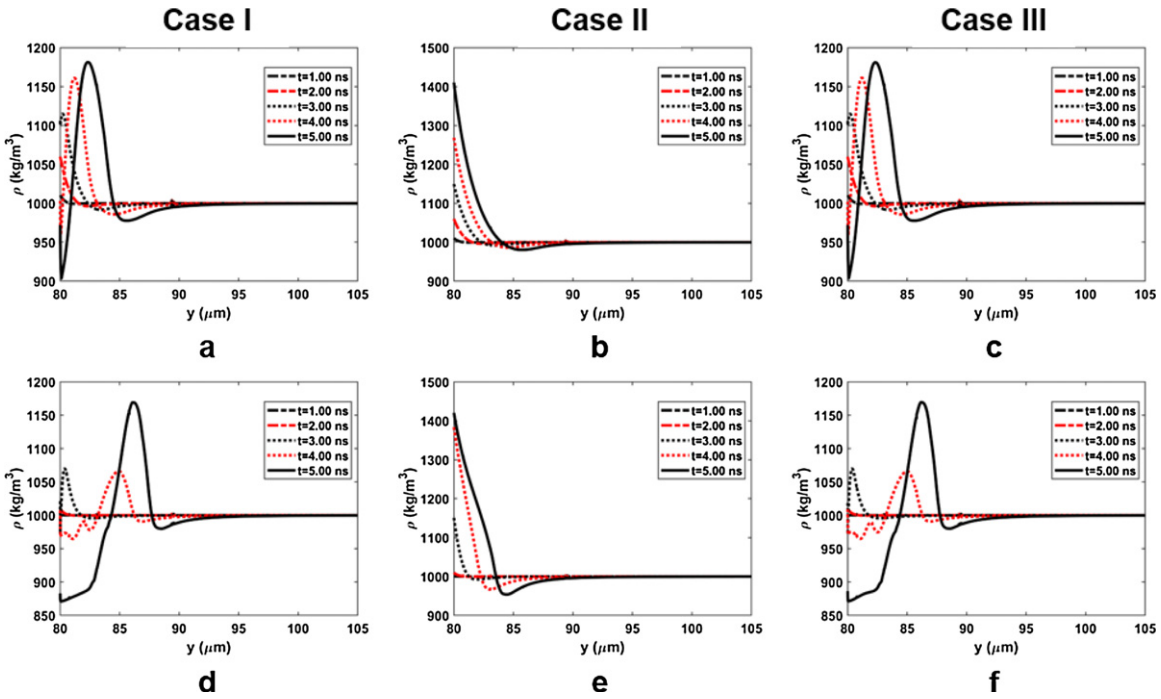

Figure 4. Temporal evolution of the centerline fluid density distribution for case I (a) and (d), case II (b) and (e) and case III (c) and (f). Viewgraphs in the top row (a)–(c) are for the linear voltage ramp and those in the bottom row (d)–(f) are under the pulsed profile.

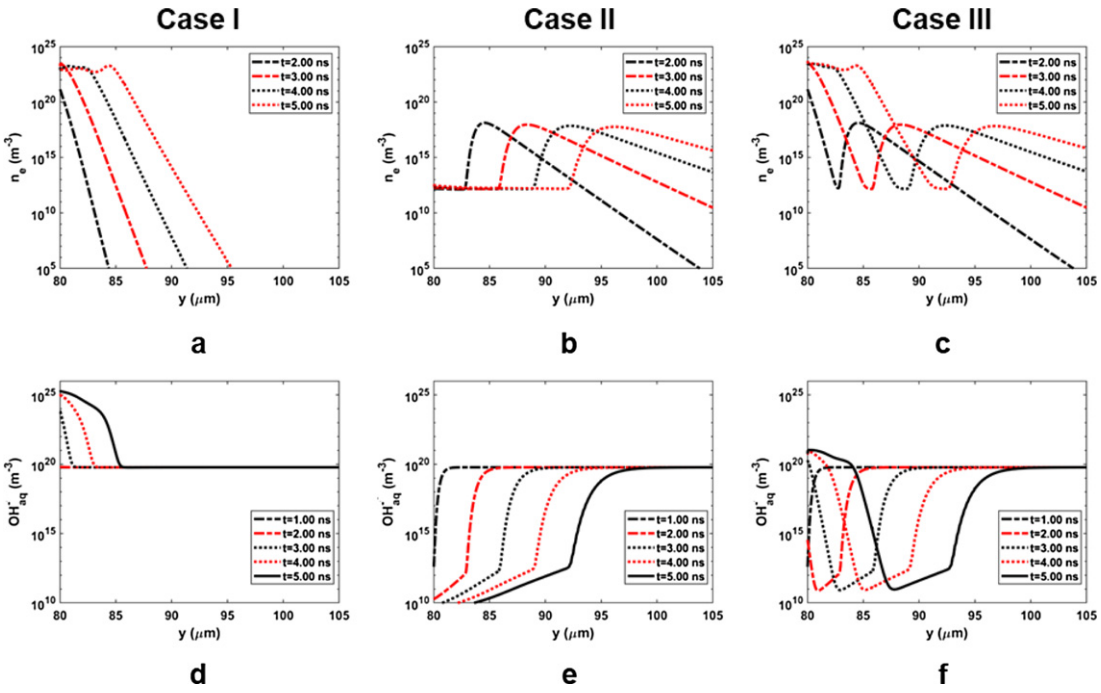

Figure 5. Evolution of the centerline electron (n_e) and OH^-_{aq} number density at different time instances for the three different cases under a linear voltage ramp.

5(a)). At 4 ns, the n_e formed only through the detachment process (case II), propagates further downstream to a distance of $\sim$10 μm. In the simultaneous presence of both R1 and R2 channels (case III), at the very initial stage, electrons are generated from the detachment reaction alone, until the available OH^-_{aq} ions near the vicinity of the powered electrode are consumed. As these electrons propagate downstream, additional electrons are produced near the powered electrode by the tunnel ionization of H_2O molecules. The spatiotemporal evolution of n_e distinctively shows the presence of a relatively weaker wave, which is followed by a stronger wave.

The H_2O ionization channel through subsequent reactions forms sufficient OH^-_{aq} ions (figure 5(d)). The number density of the negative hydroxyl ions is sufficiently high enough

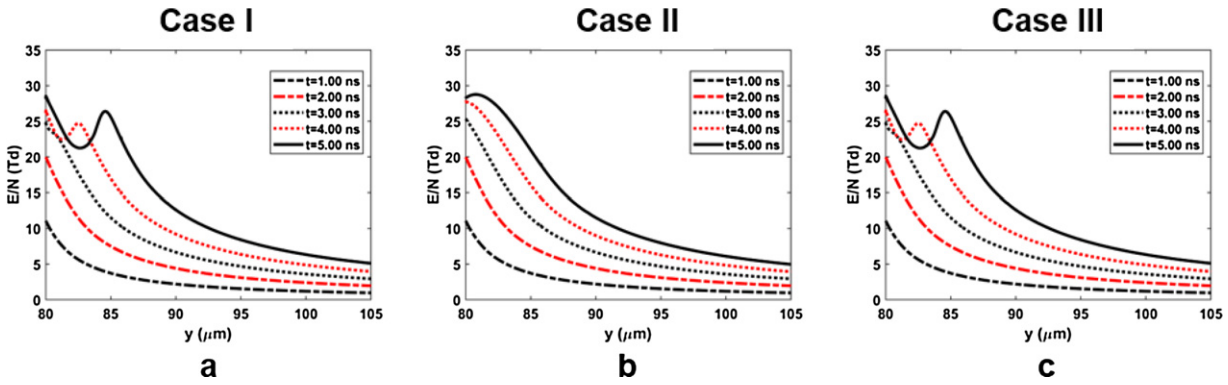

Figure 6. Variation of reduced electric ($|\mathrm{E}|/N$) along the centerline at different time instances for the three different cases under a linear voltage ramp.

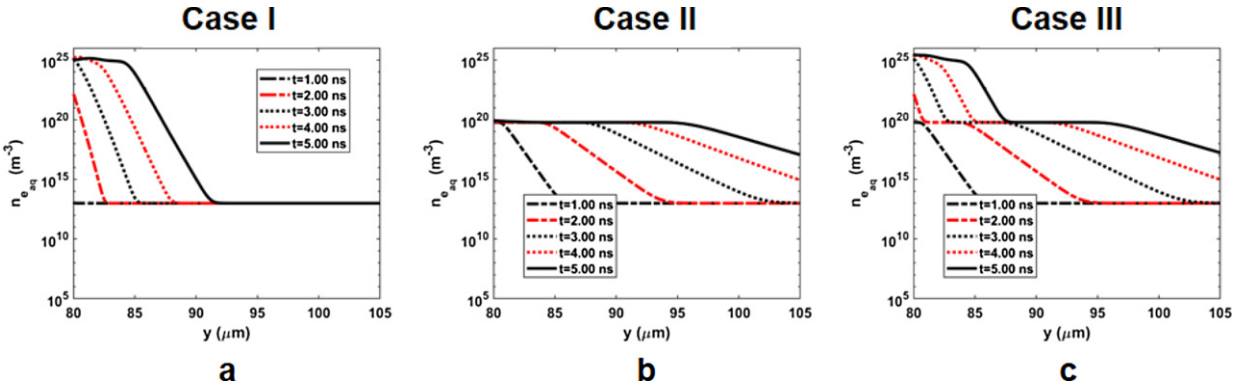

Figure 7. Evolution of solvated electron number density ($n_{e,aq}$) at the center line at different time instances for the three different cases under a linear voltage ramp.

to allow additional electrons to form through the detachment reactions (R2). For case II, the formation of electrons through detachment is sufficiently faster than the net production of OH^-_{aq}; as a result, the OH^-_{aq} gets depleted once the electrons are formed. The electron wave propagates downstream consuming the OH^-_{aq}. When both the electron sources are active (case III), the electrons formed by R1 allow the formation of sufficient OH^-_{aq} (figure 5(f)). At ∼3.0 ns, the OH^-_{aq} number density near the powered electrode increases to $\sim 1 \times 10^{20}$ m^{-3}. The subsequent n_e wave front forms at ∼3.0 ns near the powered electrode and, therefore, has contributions from both R1 and R2 channels.

Figure 6 presents the spatiotemporal evolution of the reduced electric field distribution ($|\mathbf{E}|/N$) along the centerline. In between 1–3 ns, a gradual increase in the $|\mathbf{E}|/N$ distribution takes place due to the linear increase in the applied voltage. At $t = 4$ ns, for cases I and III, where the R1 reaction is active, a localized decrease in the reduced electric field is observed close to the powered electrode (5–6 μm from the anode). Within a distance of ∼5 μm in the downstream direction the $|\mathbf{E}|/N$ value shows an increase. This undulated $|\mathbf{E}|/N$ profile is associated with the fluctuation in the density of the medium resulting from the compression and expansion waves generated in the system. With only detachment tunneling active (figure 6(b)), the $|\mathbf{E}|/N$ profiles remain free from undulation. The $|\mathbf{E}|/N$ profile does not show large variation that is associated with density changes.

The reaction mechanism contains the solvation of the plasma generated electrons to the aqueous state. The electron solvation reaction (R8) acts as one of the major loss channels for n_e. It is evident from the spatiotemporal evolution of n_e (figure 5) that as the electron generation persists for few nanoseconds the electrons are also quickly consumed. The time required for electrons to solvate is in the order of picoseconds [35]. Other reaction steps associated with electron consumption routes, such as dissociative attachment (R3–R5) and dissociative ionization (R6), are typically only active in the $|\mathbf{E}|$/N ranges above 50 Td while, for the applied voltage of 15 kV, $|\mathbf{E}|$/N barely exceeds 30 Td (figure 6).

Figure 7 shows the evolution of solvated electron number density ($n_{e,aq}$) at the centerline for the three different cases under a linear voltage ramp. By comparing the n_e and $n_{e,aq}$ profiles for case I (figures 5(a) and 7(a)), one can see that in the earlier stages when the electron generation rates are low, the electron solvation rate remains comparable to the electron production rate. As a result, most of the electrons formed during the early stage get solvated. For case II, when the electrons are generated through the detachment process alone, the generation rate is comparable to or lower than the solvation rate. As a consequence, as the electron wave propagates forward it is trailed by the region of solvated electrons (figures 5(b) and

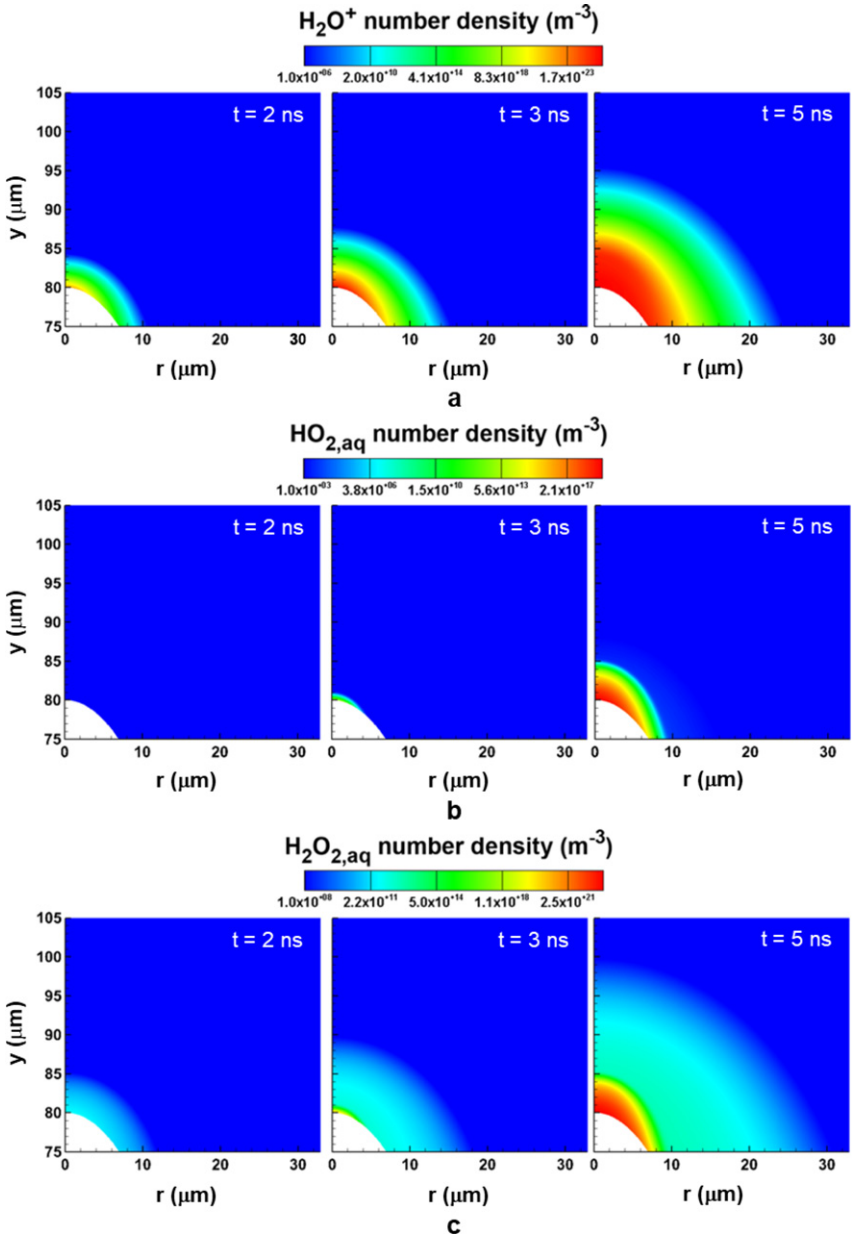

Figure 8. Spatiotemporal contour plots of (a) H_2O^+, (b) $HO_{2,aq}$ and (c) $H_2O_{2,aq}$ number density for case III under a linear voltage ramp.

7(b)) to the downstream of the electron. Once the electrons are solvated it becomes less mobile due to the lower drift and diffusion. It should be noted that reaction R30 ($H_{aq} + OH^-_{aq} \rightarrow e_{aq} + H_2O_{aq}$) also contributes to the formation of solvated electrons by converting H_{aq} and OH^-_{aq} to e_{aq} and H_2O_{aq}. R30 acts as a consumption channel of OH^-_{aq} reducing the available negative hydroxyl ions for the electron detachment process (R2). With both n_e generation channels present (i.e. reactions R1 and R2) simultaneously, during the early stages, the electrons formed from R2 get solvated; as the electric field increases and R1 is activated, a second high-concentration region of solvated electrons emerges and starts to propagate in the liquid. A distinct demarcation between these concentration levels of $n_{e,aq}$ is present due to the low diffusivity and very short time scales. It has been shown in prior works [26, 36, 37] that during water radiolysis in the absence of scavenging species like dissolved oxygen, the solvated electron density decays mainly through reaction R18. However, when considerable amounts of H_2O^+ are generated by H_2O_{aq} ionization (R1), reaction R17 also reduces e_{aq} concentration through recombination and by forming H_{aq} and OH_{aq}.

The generation of H_2O^+ ions by reaction R1 in cases I and III has a strong effect on the overall physicochemical processes of the system. As the electric field increases, the rate of reaction R1 increases dramatically and generates a considerable amount of H_2O^+ in the system. For both case I and III a peak H_2O^+ of $\sim 3.0 \times 10^{25}$ m^{-3} is attained at the end of the linear voltage ramp. Contour plots of the H_2O + for case III only is presented in figure 8. For a linear ramp, the predicted peak number densities of $HO_{2,aq}$ and $H_2O_{2,aq}$ are 1.6×10^{19} m^{-3} and 1.4×10^{23} m^{-3}, respectively (figures 8(b) and (c)).

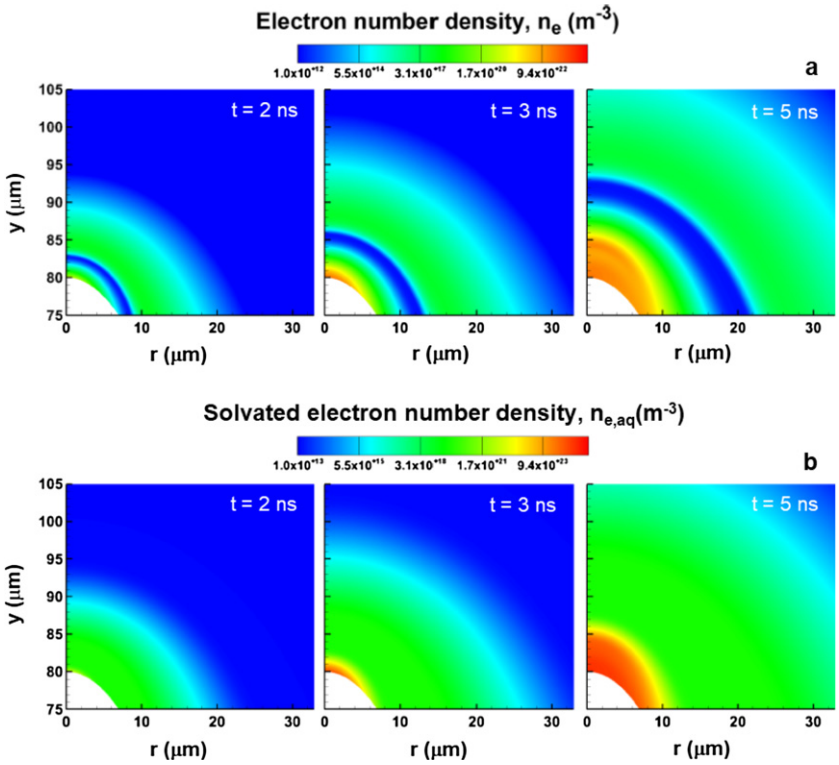

Figure 9. Spatiotemporal contour plots of (a) electrons and (b) solvated electron number density for case III under a linear voltage ramp.

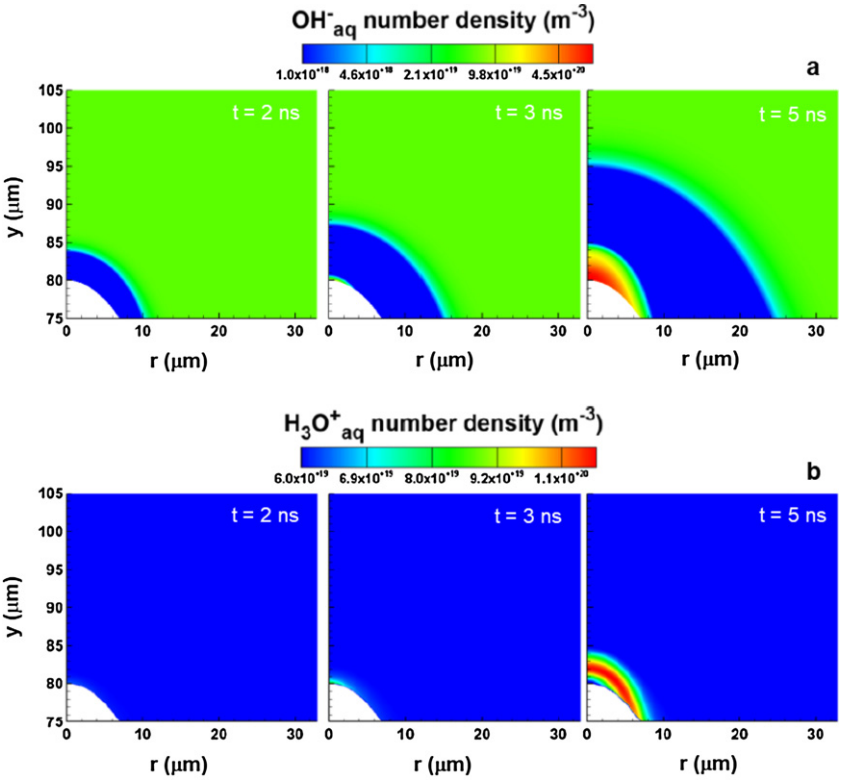

Figure 10. Spatiotemporal contour plots of (a) OH^-_{aq} and (b) $H_3O^+_{aq}$ number density for case III under a linear voltage ramp.

The contour plots of electrons, solvated electrons, OH^-_{aq} and $H_3O^+_{aq}$ at different instances for the same case are presented in figures 9 and 10. As shown in figure 9, the first wave of electrons is formed through reaction R2 at earlier times and at a lower driving voltage followed by a second ionization wave via the R1 channel. The second wave of electrons has

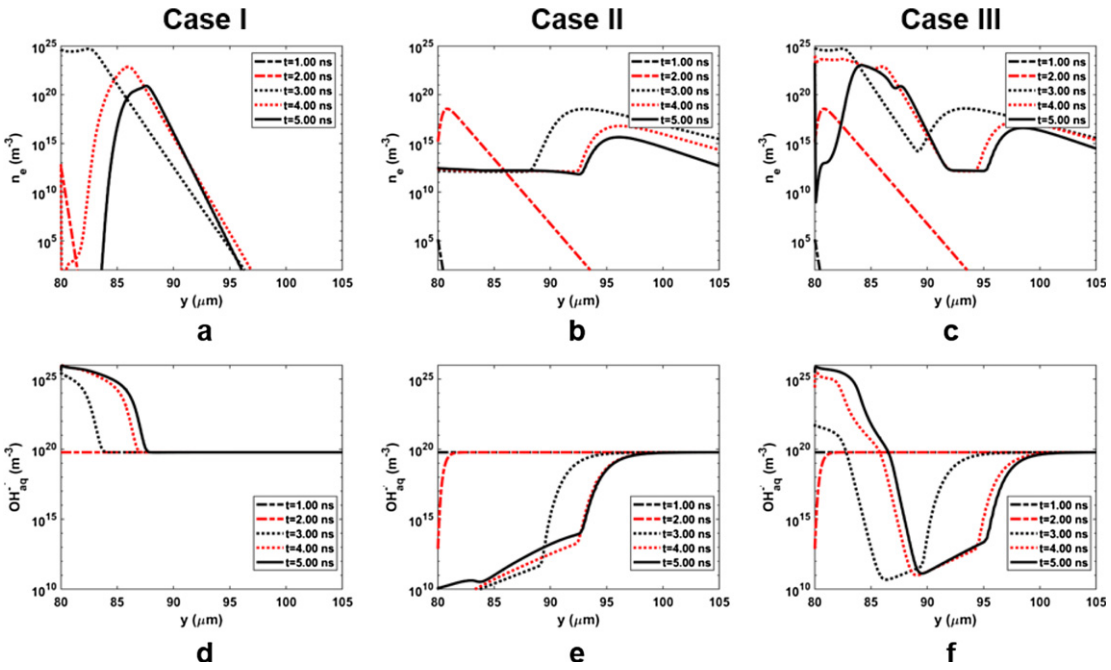

Figure 11. Evolution of the centerline electron (n_e) and OH^-_{aq} number density at different time instances for the three different cases under a pulsed voltage.

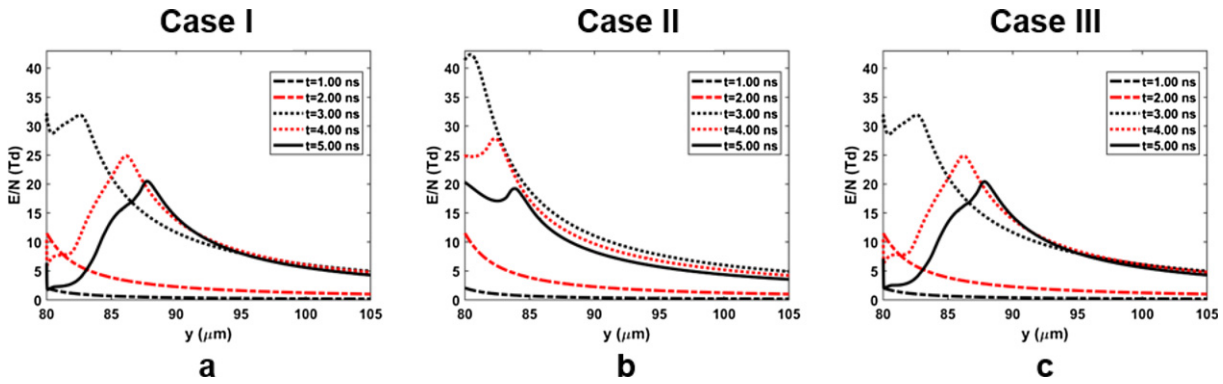

Figure 12. Variation of reduced electric ($|E|/N$) along the centerline at different time instances for the three different cases under a pulsed voltage.

a higher peak number density, despite the higher threshold energy requirement. The reaction rate for R1 depends on the number density of H_2O_{aq}, which is multiple orders of magnitude higher than that of OH^-_{aq}. As a result, once the threshold energy is acquired, the R1 channel rapidly surpasses the contribution from R2. At $t = 3$ ns, when a second electron wave emerges near the electrode surface, the electrons formed through the R2 channel propagate further downstream. The electron wave from the detachment tunneling process continues to consume the available OH^-_{aq} in the bulk medium as the wave continues to travel toward the grounded electrode (figure 10(a)). As the R1 pathway becomes active the high numbers of electrons participate in the aqueous chemistry and allow the OH^-_{aq} near the powered electrode to be replenished and augmented as time progresses. With sufficient $OH^-{}_{aq}$ present, the R2 channel becomes active together with R1 and contributes to the formation of the second wave of n_e. The $n_{e,aq}$ do not show the presence of multiple peaks. The electrons formed by both R1 and R2 continue to solvate and participate in the aqueous reactions. The predictions also show the presence of $H_3O^+_{aq}$ ions in significant amounts at the voltage ramp terminus.

The influence of the driving voltage profile is investigated by performing simulations with a pulsed voltage profile. The pulsed voltage profile has an exponential rise to V_{max} in 3 ns followed by a linear decay. The centerline distribution of n_e and OH^-_{aq} number density under the pulsed voltage for the three cases are presented in figure 11. Under the pulsed conditions, the applied voltage at 1 ns is low and, as a result, no significant electron generation is observed from either channel (figures 11(a) and (c)). As the voltage increases to ∼1.5 kV at 2 ns both the R1 and R2 reactions become active and an increase in the electron number density is observed. Compared to the linear ramp case in which, at 2 ns, the peak n_e

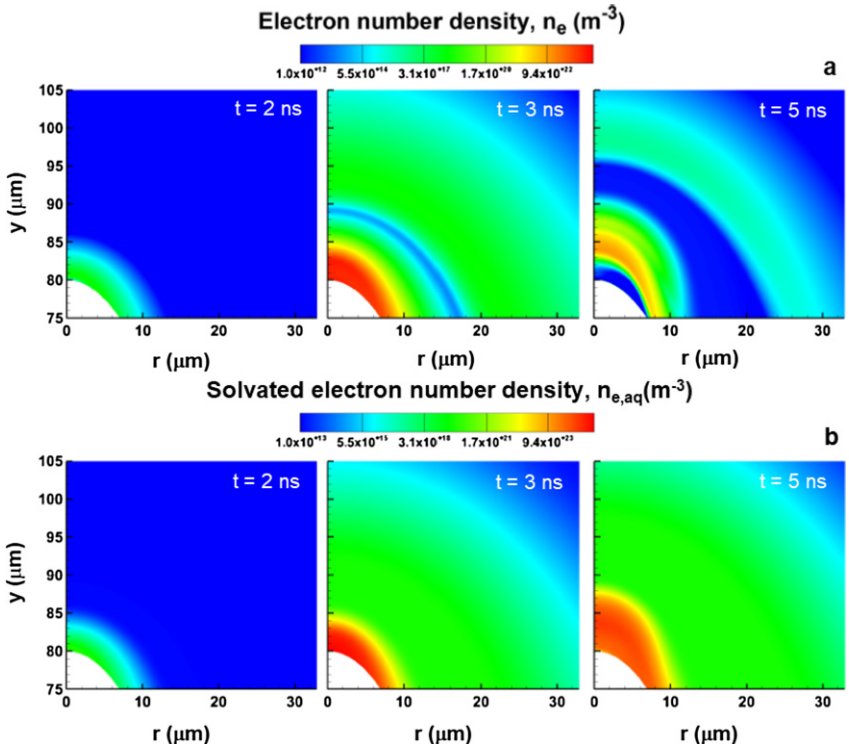

Figure 13. Spatiotemporal contour plots of (a) electrons and (b) solvated electron number density for case III under a pulsed voltage.

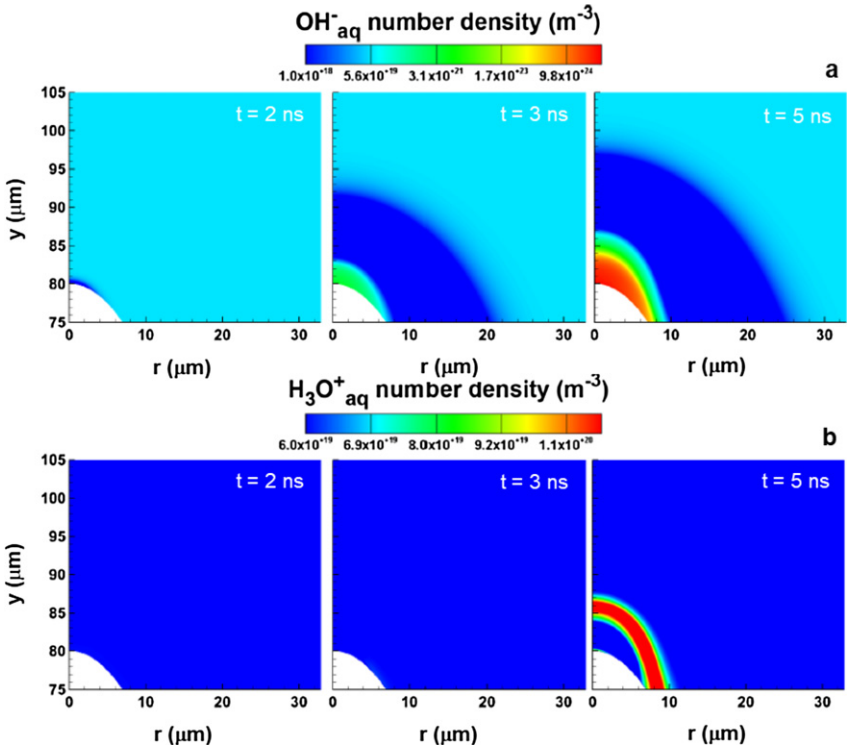

Figure 14. Spatiotemporal contour plots of (a) OH^-_{aq} and (b) $H_3O^+_{aq}$ number density for case III under a pulsed voltage.

generated from either R1 or R2 is comparable, for the pulsed case, electrons produced only from the tunnel ionization (i.e. R1 reaction) is nine orders of magnitude lower than that of R2. At 3 ns, as an ionization front is formed, n_e profiles and peak values for the ramp and pulse cases are similar. However, under pulsed conditions, the ionization front propagates further downstream. It should be noted that the voltage values for a ramp and a pulse are almost identical at 2.5 ns. After 3 ns,

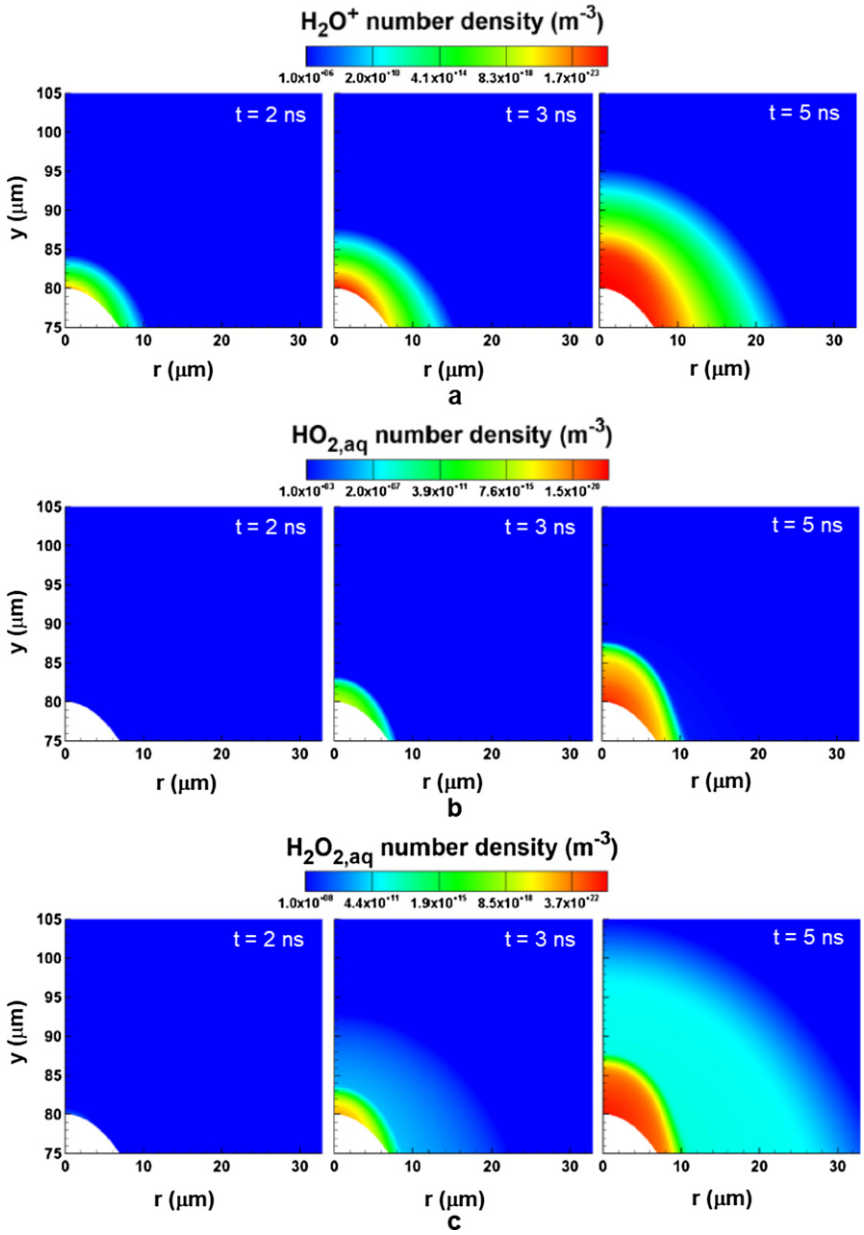

Figure 15. Spatiotemporal contour plots of (a) H_2O^+, (b) $HO_{2,\,aq}$ and (c) $H_2O_{2,aq}$ number density for case III under a pulsed voltage.

as the voltage starts to decay, the rate of reaction R1 decreases resulting in a significant decrease in the peak n_e near the powered electrode at 4 and 5 ns (figure 11(a)). From figure 11(b) it is evident that the OH^-_{aq} tunneling detachment reaction is not active until ∼2 ns. Similar to case I, under pulse conditions, the electron wave formed by R2 propagates further downstream. The R2 reaction with its lower energy barrier detaches electrons from OH^-_{aq}, even in regions far from the anode with lower field strength. Similar to the linear voltage ramp with both R1 and R2 paths active, two electron wave fronts emerge simultaneously. The first stream of n_e emerges from OH^-_{aq} detachment, which requires lower energy and is trailed by the second stream formed by R1 with a significantly higher number density. The second electron wave front, however, has contribution from both R1 and R2 reactions. It is apparent that, compared to the linear ramp, the pulsed voltage generates a significantly higher concentration of OH^-_{aq}. Therefore, in case III, the electrons produced via the R1 channel participate in the aqueous chemistry and build up the OH^-_{aq} number density near the powered electrode. As the depleted OH^-_{aq} gets replenished (figure 11(f)) the R2 reaction becomes active. It should be mentioned that under pulsed conditions the spatial lags between the two electron waves are smaller.

Similar to the linear ramp, a significant amount of OH^-_{aq} is also produced in the vicinity of the powered electrode for case I under a pulsed voltage. The OH^-_{aq} are formed by solvated electrons via reactions R16, R18–R21 and R23–R24. Most of the electrons formed by R1 get solvated and then participate in these aqueous reactions. As shown in figure 11, the OH^-_{aq} in the system is rapidly consumed to form free electrons and OH when only the R2 reaction is active. In comparison, the hydroxyl ion concentration in a linear ramp

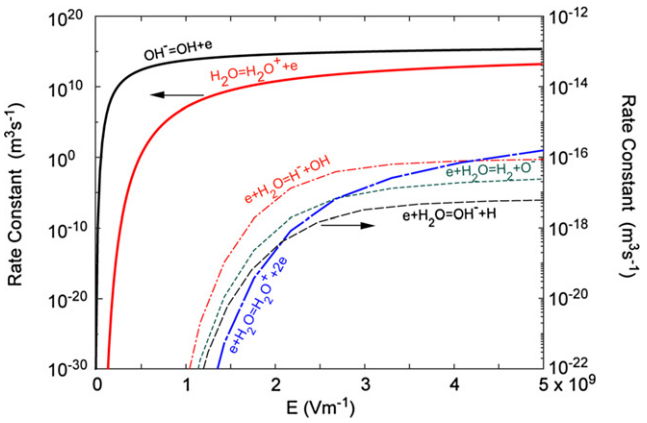

Figure 16. Reaction rate constants for R1–R6 as a function of the electric field.

decreases gradually whereas, with a pulse, the decrease is initially slow and rapid as the pulse peak approaches. Shneider and Pekker [23] estimated the number of primary electrons detached from hydroxyl ions via field ionization neglecting the secondary reactions that can recycle OH^-_{aq} in the system. They mention that in a real system in which electron-driven processes generate higher amounts of OH^-_{aq} than that which is already available from water self-ionization, reaction R2 can have a stronger influence on the breakdown process. This is evident in figure 11(f) when both R1 and R2 are simultaneously active. Near the vicinity of the powered electrode, the consumed OH^-_{aq} gets replenished and continues to grow beyond an equilibrium number density of 6×10^{19} m^{-3}. The R2 channel reactivates near the power electrode at ~3 ns as sufficient OH^-_{aq} becomes available for the tunneling detachment.

The variation in the centerline reduced electric field ($|\mathbf{E}|/N$) distribution under a pulsed driving voltage is presented in figure 12. It is apparent that the highest $|\mathbf{E}|/N$ occurs as the driving voltage reaches its peak value at 3 ns. However, the maximum $|\mathbf{E}|/N$ is not located at the powered electrode. The system experiences significant variation in density that translates to a fluctuation in the reduced electric field. Compared to the linear ramp, the system exposed to an exponential voltage rise observes higher peak $|\mathbf{E}|/N$ values.

The contour plots of n_e and $n_{e,aq}$ for the pulsed voltage are presented in figure 13. The peak n_e under the pulsed condition is $\sim 1.6 \times 10^{24}$ m^{-3}, which is a factor of 3 higher than the linear voltage ramp. As the voltage rise time gets shorter in the exponential growth, not only does the peak n_e increase at the same time, they are advected further downstream from the powered electrode. The downstream advection occurs when the driving voltage starts the linear decay. The bulk fluid velocity attains the maximum value during the voltage relaxation period (figure 3(f)). The $n_{e,aq}$ profiles clearly show the presence of stratified regions of high density $n_{e,aq}$. This is due to the low mobility and diffusivity of the solvated electrons. In regions close to the powered electrode the solvated electrons get advected as a result of the high bulk fluid velocity. Compared to n_e the $n_{e,aq}$ does not undergo a steep decrease during the voltage relaxation period.

The profiles of OH^-_{aq}, $H_3O^+_{aq}$, H_2O^+, $HO_{2,aq}$ and $H_2O_{2,aq}$ under the pulsed voltage are presented in figures 14 and 15. At $t = 3$ ns, when the driving voltage reaches its peak, the depleted OH^-_{aq} near the powered electrode gets replenished and surpasses the equilibrium OH^-_{aq} number density. The growth of OH^-_{aq} allows the R2 channel to be reactivated. The $H_3O^+_{aq}$ peak number density remains similar for both the linear ramp and pulse; however, for the pulse build up, propagation of $H_3O^+_{aq}$ occurs during the voltage decay phase. By comparing H_2O^+, $HO_{2,aq}$ and $H_2O_{2,aq}$ it is evident that the pulsed voltage generates these species at a higher concentration. The predicted peak values for H_2O^+, $HO_{2,aq}$ and $H_2O_{2,aq}$ are 1.1×10^{26} m^{-3}, 2.6×10^{22} m^{-3} and 2.5×10^{24} m^{-3}, respectively.

Figure 16 presents the rate constants for reactions R1–R6 as a function of the electric field. Reactions R1 and R2 strongly depend on the electric field magnitude, whereas R3–R6 are dependent on the reduced electric field ($|\mathbf{E}|/N$) values but, to be on the same reference, the reduced electric field dependency is rearranged to the electric field alone by multiplying by the liquid-phase neutral density. The rate constant for ionizing water molecules by Zener tunneling is lower compared to electron detachment tunneling from the negative hydroxyl ions and at the same time requires higher field strength for initiation. The Zener ionization and detachment starts to become effective, i.e. $\sim 5 \times 10^{-22}$ m^3 s^{-1} and 1×10^{-20} m^3 s^{-1} at electric field strengths of $\sim 2 \times 10^8$ Vm^{-1} and $\sim 4 \times 10^7$ Vm^{-1}, respectively. For the other electron impact ionization reactions (R3–R6) to be of a similar order an electric average electric field strength ranging in-between 1.0–1.5 $\times 10^9$ Vm^{-1} is required. The rates for both tunneling reactions (R1 and R2) are also limited by the availability of the water molecules and negative hydroxyl ions in the system. The equilibrium number density of OH^-_{aq} in distilled water is $\sim 10^{19}$ m^{-3}. However, under conducive conditions the electron-driven reactions can generate OH^-_{aq} far beyond the equilibrium concentration. For a maximum driving voltage of 15 kV, the peak OH^-_{aq} number density is predicted to be $\sim 10^{21}$ and 10^{26} m^{-3} for the ramp and pulse case, respectively. The typical number density of H_2O in distilled water is 3.3×10^{28} m^{-3}. While H_2O is abundant throughout the discharge, the OH^-_{aq} is consumed at a faster rate by R2 and requires recycling to sustain the OH^-_{aq} tunneling route. If the OH^-_{aq} number density continues to decrease, reaction R2 will cease and the electron formation will take place via R1 as long as the required electric field is available. A coupling exists between reactions R1 and R2. As long as the minimum required electric field is available, by producing sufficient electrons, R1 can replenish and sustain the OH^-_{aq} concentration in the system and keep R2 active. The electron impact dissociative attachment reactions (R3–R5) become effective at $\sim 1.8 \times 10^9$ Vm^{-1} (i.e. ~50 Td), and electron impact ionization of water (R6) requires a higher electric field and is significant at 2.5×10^9 Vm^{-1} (i.e. ~80 Td).

We conduct path flux analysis to determine the key pathways that contribute to the initial stage of the plasma formation in the liquid medium. The volume-averaged reaction rates of the dominant formation and consumption routes for electrons,

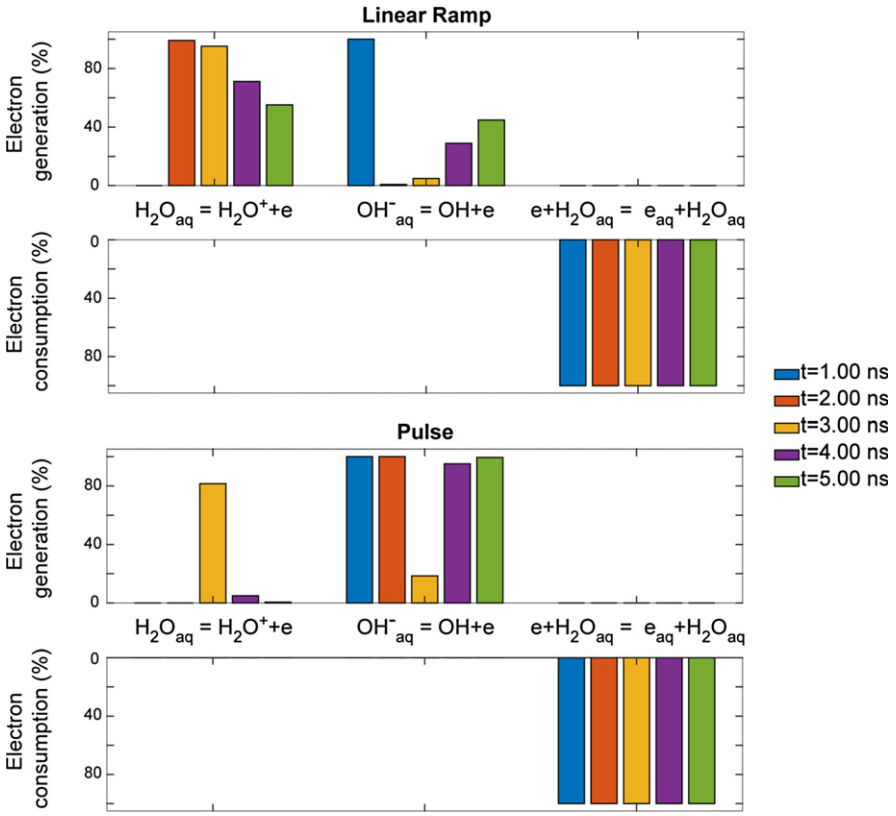

Figure 17. Volume-averaged reaction rates of the dominant formation and consumption reaction paths for electrons in case III, under both a linear ramp and pulsed voltage.

solvated electrons and negative hydroxyl radicals at different time instances for case III under a linear ramp and exponential voltage rise are summarized in figures 17–19. These rates are volume averaged over the entire solution domain and are normalized by the total rate of formation or consumption. During the initial stage (i.e. $t = 1$ ns), almost all of the electron formation is driven by R2 for both the linear ramp and pulse. At 2 ns, tunnel ionization (R1) supersedes tunnel detachment (R2) under a linear ramp, which is not the case for the pulse. Under pulsed voltage R1 surpasses R2 at $t = 3$ ns when the driving voltage reaches its maximum. At 3 ns, ∼20% of the electrons are still generated through the R2 channel. During the voltage decay phase R1 diminishes drastically but R2 remains active. In comparison, in a linear ramp after 2 ns, the contribution from R2 progressively builds up. For both conditions, as the OH^-_{aq} in the system gets replenished, the tunneling detachment remains as an active source for electrons. Electrons are predominantly consumed by hydration/solvation processes in both cases. Recombination (R7) also acts as an electron sink but is not comparable to hydration (R8). The rate of hydration in general is significantly higher than recombination. During the initial stage, recombination is negligible due to the absence of H_2O^+ ions. Even though H_2O^+ ions are formed by R1 in the later stages, the rate of the solvation reactions remains five orders of magnitude higher.

In the system, the solvated electrons are generated by two channels, $e + H_2O_{aq} \rightarrow e_{aq} + H_2O_{aq}$ (R8) and $H_{aq} + OH^-_{aq} \rightarrow e_{aq} + H_2O_{aq}$ (R30), with R8 dominating the formation rate by multiple orders of magnitude. Under the linear voltage R8 remains the major route for production of the solvated electrons. In the presence of a pulse, however, during the first nanosecond the electrons generated via R1 and R2 are extremely low (figure 11(c)); as a result, the solvation reaction R8 has a small contribution. The initial solvated electrons are formed through R30. It should be noted that even though the pathflux shows ∼90% e_{aq} formed via R30 the net e_{aq} produced during the initial stage is low. With a linear ramp, initially 55% of e_{aq} is consumed via R22 ($e_{aq} + H_3O^+_{aq} \rightarrow H_{aq} + H_2O_{aq}$), 25% by R16 ($e_{aq} + H_2O_{aq} \rightarrow H_{aq} + OH^-_{aq}$) and 15% by R18 ($2e_{aq} + 2H_2O_{aq} \rightarrow H_{2aq} + 2OH^-_{aq}$). In R22 the aqueous electrons get recombined with the hydronium ions ($H_3O^+_{aq}$) to form H_{aq} and H_2O_{aq}. The initial $H_3O^+_{aq}$ in the aqueous state is present as a product of self-ionization of water. As the concentration of $H_3O^+_{aq}$ decreases at later stages, the R22 consumption route becomes inconsequential. In R16 and R18, both these e_{aq} consumption channels contribute to the formation of OH^-_{aq} in the system. As the system approaches 4 ns, R17 ($e_{aq} + H_2O^+_{aq} \rightarrow H_{aq} + OH_{aq}$), R18 and R19 ($e_{aq} + H_{aq} + H_2O_{aq} \rightarrow H_{2aq} + OH^-_{aq}$) and R20 ($e_{aq} + OH_{aq} \rightarrow OH^-_{aq}$) become the main e_{aq} consumption reactions. Reactions R18–R20 all contribute to the formation of OH^-_{aq} and, in R19 and R20, e_{aq} reacts with water. This suggests that if enough solvated electrons are present, sufficient OH^-_{aq} will be formed and can easily act as the source for electrons during the voltage decay stage.

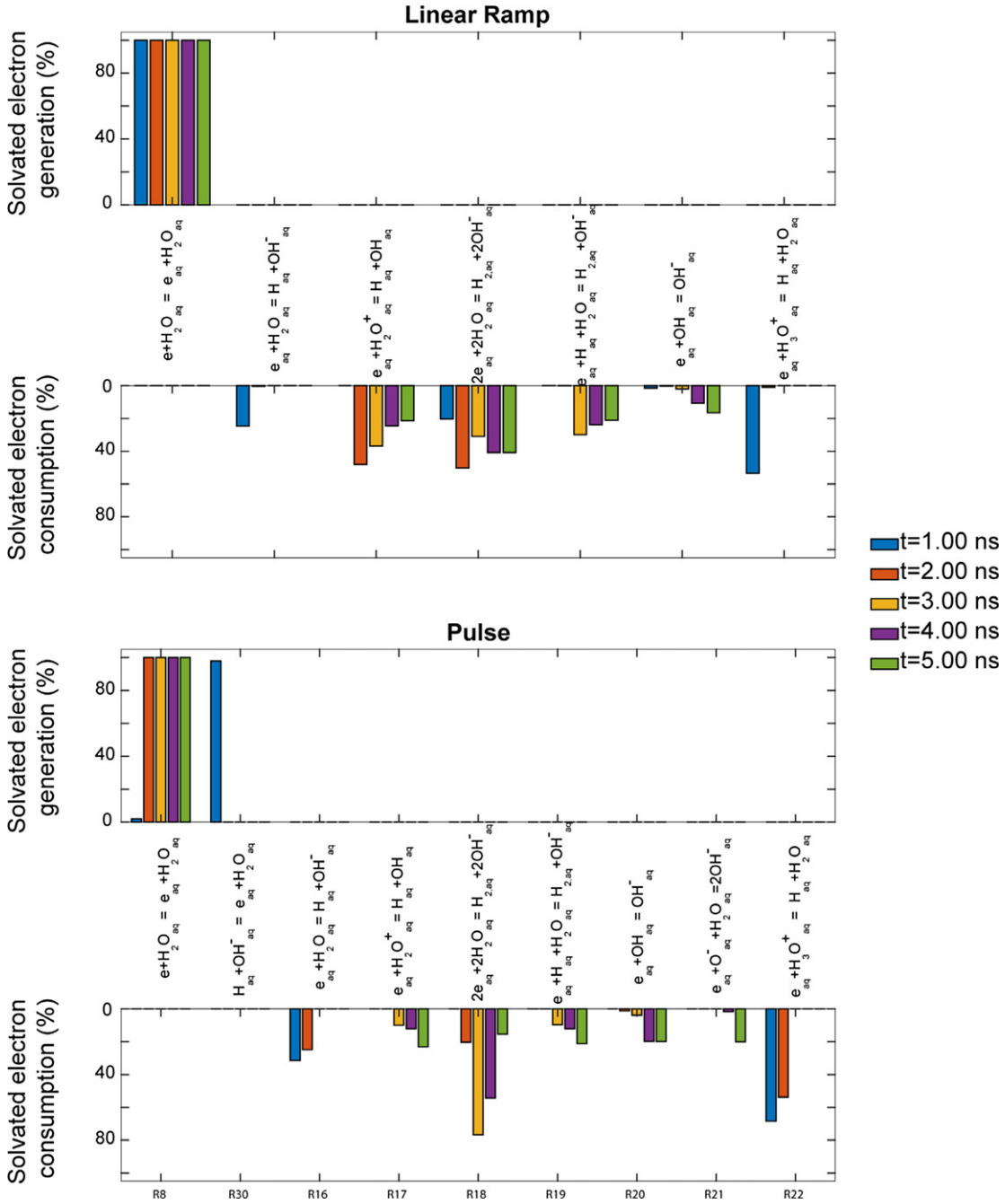

Figure 18. Volume-averaged reaction rates of the dominant formation and consumption reaction paths for solvated electrons in case III, under both a linear ramp and pulsed voltage.

Unlike the linear ramp, during the voltage pulse, R22 and R16 are established as the major consumption routes for e_{aq}, contributing to ∼65% and 32% of the total consumption. R18 also becomes active only at 2 ns and increases to ∼78% at 3 ns. As the voltage enters the linear decay phase, consumption through R18 starts to decrease and R17, R19 and R20 start taking over. At $t = 5$ ns, R17, R19–R21 and R18 consume 23%, 21%, 20%, 20% and 15% of aqueous electrons, respectively.

Figure 19 presents the volume-averaged reaction rates of the formation and consumption routes of OH^-_{aq} at different time instances. Hydroxyl ion consumption through tunneling detachment remains a dominant path for the entire voltage duration. R52 ($H_3O^+_{aq} + OH^-_{aq} \rightarrow H_{aq} + OH_{aq} + H_2O_{aq}$) is active at early times only under pulsed conditions. The concentration of $H_3O^+_{aq}$ is the limiting factor for this reaction as both R52 and R22 compete for the $H_3O^+_{aq}$ pool and the generation of H_3O^+ by R51 and R53 is relatively slow. At 1 ns, 54% and 43% of hydroxyl ions are formed through reactions R16 and R18 and only 3% is formed by R20.

As time progresses, a sharp increase is observed in production of OH^-_{aq} by reactions R18–R20. These reactions generate 52%, 27% and 21% of the total OH^-_{aq} production, respectively. Similar to prior works [26, 36, 37], R18 is found to be the major

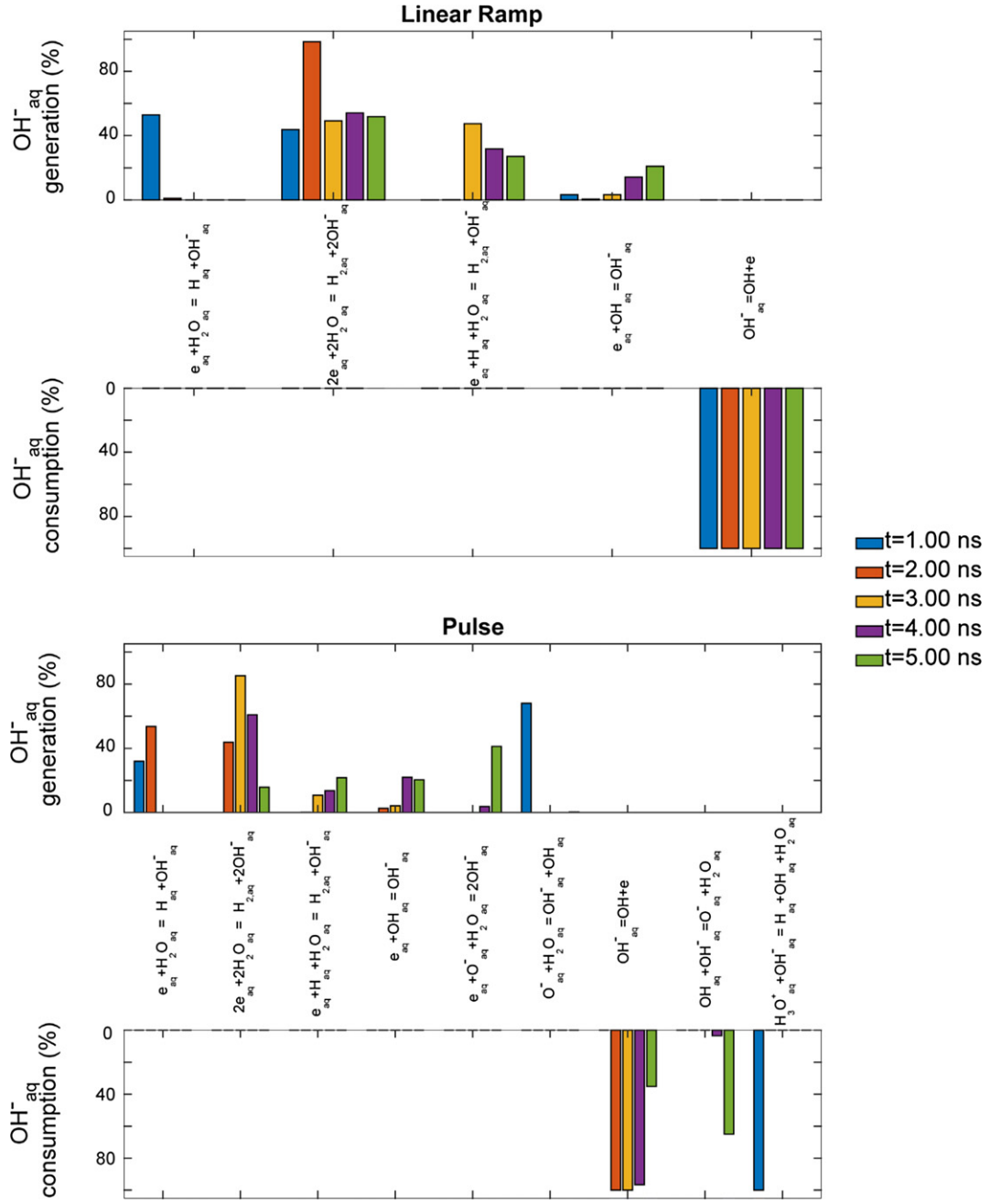

Figure 19. Volume-averaged reaction rates of the dominant formation and consumption reaction paths for negative hydroxyl ions in case III, under both a linear ramp and pulsed voltage.

sink of e_{aq} and source of OH^-_{aq}. The comparison further shows that R19 and R20 are not initially significant since the H and OH radicals necessary to proceed are not available in sufficient quantities. The OH radicals are formed later by electron-driven reactions, namely R12 and R17. At 5 ns, 33% and 66% of the OH_{aq} is formed by R12 and R17, respectively. The hydroxyl radical produced in R2 gets solvated in water by R12 and is the only source of OH_{aq} at earlier times but, as the OH^-_{aq} concentration decreases, less OH_{aq} becomes available as well. On the other hand, as the electron number density increases at later times, the R17 dissociative recombination reaction becomes the dominant source for OH_{aq} radicals. From 2 to 5 ns, almost all of the H_{aq} radicals are produced by R17, whereas between 0–2 ns, R52 acts as the main source.

For the pulse, R16 ($e_{aq} + H_2O_{aq} \rightarrow H_{aq} + OH^-_{aq}$) and R43 ($O^-_{aq} + H_2O_{aq} \rightarrow OH^-_{aq} + OH_{aq}$) reactions generate the negative hydroxyl ions during the early stage (i.e. 1 ns) contributing to ∼31% and 65% of the overall production. It should be noted that the overall rate of production of OH^-_{aq} during this stage is small. From 2 ns onward, R16 ($e_{aq} + H_2O_{aq} \rightarrow H_{aq} + OH^-_{aq}$) and R18 ($2e_{aq} + 2H_2O_{aq} \rightarrow H_{2aq} + 2OH^-_{aq}$) become the major contributing reactions as sufficient solvated electrons become available. While at 2 ns, ∼53% of hydroxyl ions are produced by R16, the contribution becomes insignificant at 3 ns,

whereas the contribution from R18 continues to increase and reaches ∼85%. OH^-_{aq} formation via R19 ($e_{aq} + H_{aq} + H_2O_{aq} \rightarrow H_{2aq} + OH^-_{aq}$), R20 ($e_{aq} + OH_{aq} \rightarrow OH^-_{aq}$) and R21 ($e_{aq} + O^-_{aq} + H_2O_{aq} \rightarrow 2OH^-_{aq}$) is not prevalent until the maximum voltage is attained in the pulse. At 4 ns, 22%, 21% and 41% of hydroxyl ions are formed by R19–R21, respectively, while only 16% is generated by R18. The overall rate of formation of OH^-_{aq} has its highest value at $t = 4$ ns. For the linear ramp R2 remains the major consumption reaction for the entire time duration. In comparison, for the pulse in-between $t = 2$–4 ns, R2 remains the dominant pathway; however, at 5 ns, the contribution of R2 decreases to ∼32% and R40 ($OH_{aq} + OH^-_{aq} \rightarrow O^-_{aq} + H_2O_{aq}$) consumes ∼64% of OH^-_{aq}.

6. Conclusions

A multiphysics model together with an extended kinetic mechanism have been employed to identify the role of negative hydroxyl ions in liquid-phase plasma initiation. Two competing tunneling mechanisms were considered—ionization of water molecules and electron detachment from negative hydroxyl ions available in liquid water. The simulations were conducted for a powered needle-like electrode for two different driving-voltage profiles—one with a linear rise time and another with an exponential nanosecond rise time. A peak voltage of 15 kV was considered for both voltage profiles. Parametric simulations were conducted to isolate the physicochemical processes occurring due to the two different tunneling routes in these very short time scales. The results from the simulations have shown that the tunneling detachment of electrons is very active during the initial stages as it has a low threshold energy requirement. The hydrodynamics associated with the OH^-_{aq} detachment tunneling were distinctively different compared to the tunneling ionization. The electrical forces during the detachment tunneling processes were found to generate a stronger compression but a weaker expansion regime in the liquid. The liquid experiences a ∼40% increase and ∼1% decrease in its density. The predictions showed that the tunnel ionization generates stronger electrostatic, polarization and electrostrictive ponderomotive forces, and larger variations in density are observed and are especially associated with expansion. Even though the electrostrictive ponderomotive forces contribute to the very initial phase of the density variation through tensile stresses, polarization and electrostatic forces also contribute as the discharge initiation progresses. The smallest density change allows the polarization force to be effective as it depends on the gradient of the dielectric permittivity, which is a function of the medium density. With ionization the electrostatic forces driven by the charged species have a strong impact as well. When both tunneling processes were present, the hydrodynamics were strongly dictated by the ionization as significantly higher charged species are generated once the threshold electric field becomes available. Two propagating waves of electrons emerge in the system in which the electrons generated from the detachment tunneling precede the field ionization. The peak electrons generated through detachment are 5–6 orders of magnitude lower than those generated by field ionization. However, the predictions indicated that as sufficient negative hydroxyl ions are present in the system, the detachment remains prevalent even at a low electric field—during the voltage decay phase. The prediction also shows that the reduced electric field is not sufficient enough to allow electron impact ionization to be active and make a significant contribution. It should be noted that the tunneling from OH^-_{aq} does not decrease the density to the extent that is representative of nanovoids. The field ionization, which creates higher numbers of charged species, can contribute to and enhance the cavitation of the liquid medium via the electrostatic force and can augment nanovoid regions in the fluid.

Path flux analysis indicated that for an exponential pulse the field ionization becomes dominant when the driving voltage reaches its maximum. The majority of the electrons are produced from negative hydroxyl ions during the pre-rise and the decay phase. The OH^-_{aq} in the system gets quickly depleted in regions where the detachment occurs and becomes a rate-limiting condition. Solvated electrons contribute to the replenishment of the negative hydroxyl ions through the liquid-phase reactions. These OH^-_{aq} are formed near the powered electrode and allow generation of additional streams of electrons. A strong and coupled recycling of the negative hydroxyl ions will allow both tunneling processes to remain active throughout the initiation process of the discharge.

Data availability statement

All data that support the findings of this study are included within the article (and any supplementary files).

Acknowledgments

The work reported is supported by the Division of Physics of the US National Science Foundation under Grant No. 1707282.

ORCID iDs

Tanvir Farouk https://orcid.org/0000-0002-5579-0949

References

[1] Bruggeman P J *et al* 2016 *Plasma Sources Sci. Technol.* **25** 053002
[2] Bruggeman P and Leys C 2009 *J. Phys. D: Appl. Phys.* **42** 053001
[3] Levchenko I, Bazaka K, Baranov O, Sankaran M, Nomine A, Belmonte T and Xu S 2018 *Appl. Phys. Rev.* **5** 021103
[4] Mizuno T, Ohmori T, Akimoto T and Takahashi A 2000 *Japan. J. Appl. Phys.* **39** 6055–61
[5] Horikoshi S and Serpone N 2017 *RSC Adv.* **7** 47196–218
[6] Hamdan A and Cha M S 2016 *AIP Adv.* **6** 105112
[7] Foster J, Sommers B S, Gucker S N, Blankson I M and Adamovsky G 2012 *IEEE Trans. Plasma Sci.* **40** 1311–23

[8] Ceccato P H, Guaitella O, Le Gloahec M R and Rousseau A 2010 *J. Phys. D: Appl. Phys.* **43** 175202
[9] Marinov I, Guaitella O, Rousseau A and Starikovskaia S M 2013 *Plasma Sources Sci. Technol.* **22** 042001
[10] Seepersad Y, Pekker M, Shneider M N, Fridman A and Dobrynin D 2013 *J. Phys. D: Appl. Phys.* **46** 355201
[11] Pongrác BŠimek M, Člupek M, Babický V and Lukeš P 2018 *J. Phys. D: Appl. Phys.* **51** 124001
[12] Grosse K, Schulz-von der Gathen V and von Keudell A 2020 *Plasma Sources Sci. Technol.* **29** 095008
[13]Šimek M, Pongrác B, Babický V, Člupek M and Lukeš P 2017 *Plasma Sources Sci. Technol.* **26** 07LT01
[14] Dobrynin D, Seepersad Y, Pekker M, Shneider M, Friedman G and Fridman A 2013 *J. Phys. D: Appl. Phys.* **46** 105201
[15] Keudell A, Grosse K and Schulz-von der Gathen V 2020 *Plasma Sources Sci. Technol.* **29** 085021
[16] Joshi R P, Qian J, Zhao G, Kolb J, Schoenbach K H, Schamiloglu E and Gaudet J 2004 *J. Appl. Phys.* **96** 5129–39
[17] Shneider M, Pekker M and Fridman A 2012 *IEEE Trans. Dielectr. Electr. Insul.* **19** 1579–82
[18] Sharbaugh A H, Devins J C and Rzad S J 1978 *IEEE Trans. Dielectr. Electr. Insul.* **EI-13** 249–76
[19] Devins J C, Rzad S J and Schwabe R J 1981 *J. Appl. Phys.* **52** 4531–45
[20] Qian J, Joshi R P, Schamiloglu E, Gaudet J, Woodworth J R and Lehr J 2006 *J. Phys. D: Appl. Phys.* **39** 359–69
[21] Aghdam A C and Farouk T 2020 *Plasma Sources Sci. Technol.* **29** 025011
[22] Kolb J F, Joshi R P, Xiao S and Schoenbach K H 2008 *J. Phys. D: Appl. Phys.* **41** 234007
[23] Shneider M and Pekker M 2016 *Liquid Dielectrics in an Inhomogeneous Pulsed Electric Field* (Bristol: IOP Publishing)
[24] Li Y-H 1967 *J. Geophys. Res.* **72** 2665–78
[25] Hagelaar G J M and Pitchford L C 2005 *Plasma Sources Sci. Technol.* **14** 722–33
[26] Schmidt K H, Han P and Bartels D 1992 *J. Phys. Chem.* **96** 199–206
[27] Atkins P and de Paula J 2002 *Physical Chemistry* 7th edn (San Francisco, CA: Freeman)
[28] Cusseler E L 1997 *Diffusion: Mass Transfer in Fluid Systems* (Cambridge: Cambridge University Press)
[29] Tian W and Kushner M J 2014 *J. Phys. D: Appl. Phys.* **47** 165201
[30] Itikawa Y and Mason N 2005 *J. Phys. Chem. Ref. Data* **34** 1–22
[31] Weller H G, Tabor G, Jasak H and Fureby C 1998 *Comput. Phys.* **12** 620
[32] Ren Z and Pope S B 2008 *J. Comput. Phys.* **227** 8165–76
[33] Strang G 1968 *SIAM J. Numer. Anal.* **5** 506–17
[34] Hindmarsh A C, Brown P N, Grant K E, Lee S L, Serban R, Shumaker D E and Woodward C S 2005 *ACM Trans. Math. Softw.* **31** 363–96
[35] Chase W J and Hunt J W 1975 *J. Phys. Chem.* **79** 2835–45
[36] Rumbach P, Bartels D M, Sankaran R M and Go D B 2015 *Nat. Commun.* **6** 7248
[37] Buxton G V, Greenstock C L, Helman W P and Ross A B 1988 *J. Phys. Chem. Ref. Data* **17** 513–886